Atmospheric corrosion of iron under a single droplet

A new systematic multi-electrochemical approach

Rahimi, Ehsan; Zhang, Keer; Kosari, Ali; Van den Steen, Nils; Homborg, Axel; Terryn, Herman; Mol, Arjan; Gonzalez-Garcia, Yaiza

DOI
10.1016/j.corsci.2024.112171

Publication date
2024

Document Version
Final published version

Published in
Corrosion Science

Corrosion Science 235 (2024) 112171

Contents lists available at ScienceDirect

Corrosion Science

journal homepage: www.elsevier.com/locate/corsci

Atmospheric corrosion of iron under a single droplet: A new systematic multi-electrochemical approach

Ehsan Rahimi [a,*,1,2], Keer Zhang [a], Ali Kosari [a], Nils Van den Steen [b], Axel Homborg [a,c], Herman Terryn [b], Arjan Mol [a], Yaiza Gonzalez-Garcia [a]

[a] Delft University of Technology, Department of Materials Science and Engineering, Mekelweg 2, Delft, CD 2628, the Netherlands
[b] Research Group Electrochemical and Surface Engineering, Vrije Universiteit Brussel, Pleinlaan 2, Brussels 1050, Belgium
[c] Netherlands Defence Academy, Het Nieuwe Diep 8, Den Helder, AC 1781, the Netherlands

ARTICLE INFO

Keywords:
Atmospheric corrosion
Single Droplet
Micro-electrodes, Electrochemical noise
Oxygen diffusion
Localized corrosion

ABSTRACT

Utilizing a dedicated micro-sized three-electrode cell, this study systematically investigates early-stage electrochemical properties and corrosion behavior of pure iron under single droplets. Various volumes and NaCl concentrations were considered during the evaporation-driven shape and concentration evolution of single droplets. The measurements disclosed that reducing the droplet size from 5 μL to 1.5 μL at 0.01 M NaCl concentration, increased noise resistance (R_n) and polarization resistance (R_p) values. However, at 0.1 M and 0.2 M NaCl concentrations, reducing droplet size led to the domination of relatively high chloride ion concentration over oxygen diffusion, resulting in a very low R_n and R_p, and hence enhanced localized corrosion.

1. Introduction

The prevention of gradual deterioration of metallic materials through exposure to an atmospheric environment remains a challenge for many structural and functional applications [1]. Not only is their chemical stability compromised by corrosion, but their mechanical properties may also be at stake depending on in-service corrosive and loading conditions. Examples are stress corrosion cracking [2], corrosion fatigue [3], and hydrogen embrittlement [4]. Single or multiple droplets and/or thin electrolyte film can be formed owing to rain, snow, and dew condensation, which causes a uniform or local corrosion process on metallic materials [5]. Particularly, the shape (hemispherical or spherical [6]) and thickness evolutions of the single droplet or thin electrolyte film strongly affect the number of the chemo-physical processes such as type and accumulation of the corrosion products, mass transport of dissolved oxygen and the hydration of released metal ions [7–9]. The atmospheric corrosion rate of metallic materials depends on the height or thickness of a single droplet or thin electrolyte film, respectively [9]. This further affects the oxygen gas transport and its diffusion process to the electrolyte, resulting in different rates and types of the cathodic reduction reaction (e.g. under activation control or polarization control - e.g. limiting diffusion current density) [10–12]. Therefore, these different kinds of cathodic reduction reactions in neutral or alkaline environments influence the rate of the anodic dissolution process [9]. Likewise, the gradual evaporation of a saline droplet generates an increase in the concentration of anions in the droplet (e.g. Cl^-, CO_3^{2-}, SO_4^{2-}, etc.). This dynamic evaporation subsequently accelerates the metal ion release and reduces the pH due to an increased hydrolyzation of metal ions [13,14].

Over the last two decades, numerous approaches have been developed to record the electrochemical response, surface microstructure/morphology, and chemical composition of metallic materials under a single droplet and/or thin electrolyte film. These were divided based on two main setups such as electrochemical tests or scanning probe microscopy (SPM). These investigations were considered since traditional corrosion tests utilizing electrochemical analyses and/or simulating a harsh corrosive medium (e.g. salt spray chamber), denoted as accelerated corrosion tests, cannot precisely assess the real corrosion resistance behavior of all metals or alloys [15]. For instance, the single droplet electrochemical tests can be described using a quasi-counter reference

* Correspondence to: Department of Materials Science and Engineering, Corrosion Technology and Electrochemistry (CTE), Delft University of Technology, Delft, CD 2628, the Netherlands.
E-mail address: e.rahimi-2@tudelft.nl (E. Rahimi).
[1] ORCID ID: 0000-0002-7128-8940
[2] Google scholar: https://scholar.google.com/citations?user=pNVxwcYAAAAJ&hl=enWeb of Science Researcher ID: I-8386-2019

https://doi.org/10.1016/j.corsci.2024.112171
Received 9 February 2024; Received in revised form 22 May 2024; Accepted 1 June 2024
Available online 6 June 2024

electrode (QCRE). This technique was employed to measure the corrosion behaviour of metals or alloys using potentiodynamic polarization (destructive test) and/or electrochemical impedance spectroscopy (EIS) measurements (non-destructive test) by approaching the syringe containing droplet to the studied surface. Some previous studies with this approach on metallic materials were focused on ultra-pure iron [13], copper (Cu)[16], aluminum (Al)[16], carbon steel, and galvanized steel [17]. Other studies utilized wire beam electrodes or multi-wires techniques to monitor and map the electrochemical current signals (e.g. for zinc (Zn) [6] and pure iron [14]). Nevertheless, employing the QCRE method can notably alter the actual size of the droplet volume and its shape, reduce the droplet surface area and an imprecise/artificial gradient of oxygen diffusion supported by reservoir pressure, which is away from the reality of the atmospheric environment [18]. These two last undesirable events, alongside the capillary effect in the silicon gasket/solid surface interface, can also happen in the electrochemical micro-cell or scanning micropipette contact method [19]. Those techniques based on SPMs include ex- or in-situ atomic force microscopy (AFM) and Kelvin probe force microscopy (KPFM) study of Mg [20] and steel [21], scanning electrochemical microscopy (SECM) [22] study of Cu/Al interface under a thin electrolyte film.

Since in the natural atmosphere, the thickness of the formed thin electrolyte or single droplet is time-dependent due to condensation and most notably evaporation phenomena [23], a dynamic thickness/shape evolution of electrolyte/droplet and electrochemical interactions will occur that considerably influences the rate and type of corrosion process.

In this research, a systematic approach was established to visualize the early-stage dynamic shape and electrochemical signal evolutions of a pure iron surface under a single droplet with different sizes (1.5 μL, 3 μL, and 5 μL) and NaCl concentrations (0.01 M, 0.1 M, and 0.2 M). A combination of DC and AC multi-electrochemical analyses was considered using a tailor-made micro-sized three-electrode cell incorporating potentiodynamic polarization (PDP) and electrochemical impedance spectroscopy (EIS) measurements. Moreover, a new approach was conducted to obtain the electrochemical current and potential noise (ECN and EPN) signals (e.g. corrosion evolutions [24–28]) of the pure iron alongside ECN time-frequency mappings during the dynamic evolution of a single droplet.

2. Experimental procedure

2.1. Materials and reagents

To create the micro-sized three-electrode cell, pure iron (99.99 %, Fe005816, Goodfellow), silver (99.99 %, Ag005127, Goodfellow), and platinum (99.9 %, 43772-Alfa Aesar) wires with diameters of 0.2 mm were purchased. The NaCl solutions with different concentrations (0.01 M, 0.1 M, and 0.2 M) were prepared using ultra-pure water (Milli-Q ix7003, > 5 MΩ.cm) and NaCl salt (J.T.Baker™). Using a pH meter and solution conductivity meter, the pH and conductivity values of three different NaCl solutions including 0.01 M, 0.1 M, and 0.2 M were measured and values are obtained in Table 1.

2.2. Camera and surface microstructural characterization

To measure and analyze the volume, surface area, and contact angle of the hemispherical droplet during droplet evaporation and electrochemical analysis, the droplet images were processed by Image J (Drop Analysis LB-ADSA module) software. In addition, a scanning electron microscope (SEM, Jeol JSM-IT100) equipped with an energy-dispersive X-ray spectroscopy (EDXS) detector was utilized to visualize the microstructure and study the chemical composition of the micro-sized Ag/AgCl reference electrode (RE). The SEM and EDXS surface analyses were collected at an accelerated voltage of 20 keV and in secondary electrons (SE) mode. Raman analysis was conducted with an Invia Reflex Raman spectroscope from Renishaw Scientific. The formed Fe corrosion products were analyzed using a green laser with an excitation wavelength of 514 nm and a spot 5 μm in size on the specimen.

Table 1
The pH and conductivity values of various NaCl concentrations.

NaCl concentration (M)	pH	Conductivity (S/cm)
0.01	6.7	0.95
0.1	5.9	4.8
0.2	5.6	17.8

2.3. Designing the different micro-sized three-electrode cells and surface characterization

Two different types of micro-sized three-electrode cells were considered for all electrochemical measurements. Firstly, the electrochemical noise (EN) type uses two identical pure iron wires as working electrodes (WE, number #1 and #2) plus one micro-sized Ag/AgCl reference electrode (RE). Secondly, the potentiodynamic polarization (PDP) and electrochemical impedance spectroscopy (EIS) type, uses one iron wire as WE, a platinum wire as a counter electrode (CE), and a micro-sized Ag/AgCl as RE. The schematic pictures in Fig. 1**a and** 1**b** present these different types of micro-sized three-electrode cells alongside the electrode configuration. A macrograph image of a micro-sized three-electrodes cell in cold mounting is also shown in Fig. 1**c**. With this configuration, the shape of the droplet, when spread over the surface, does not disturb the electrochemical measurements and oxygen diffusion process within the droplet.

As represented in Fig. 1**c**, an Ag/AgCl electrode is located in the center between the two iron wires. This micro-sized Ag/AgCl electrode was fabricated by anodically polarizing the Ag wire in a 0.1 M NaCl solution for a duration of 1 hour to form a layer of AgCl around the Ag wire, as a core-shell electrode (SEM and corresponding EDXS elemental maps and spectrum are shown in Fig. 1**d**). The potential of our designed reference electrode turned out to be very stable during the measurements. The surface roughness distribution of the Fe surface for all electrochemical analyses was examined using a Bruker Dimension Edge™ instrument in a tapping mode condition (TESPA-V2 probe, with a height and tip radius of 10–15 μm and 7 nm, respectively). The mean surface roughness was ~ 356 nm (root mean square roughness, Rq = 69.5 nm), as presented in the topography and its corresponding histogram analysis in Figs. 1**e and** 1**f**. Comparing offset potential differences, the potential value for the small Ag/AgCl electrode starts at 5 mV and decreases to ~6.5 mV with 1.5 mV instability after 1 hour (Fig. 2**a**). Considering the total monitoring time of 30-minutes, the offset potential difference, including 1 mV instability, is ~6 mV. Moreover, the micro-sized Ag/AgCl reference electrode exhibits a noise level of 0.6 mV to 0.8 mV, which is deemed acceptable given the much larger dynamic range of the potential signals in all electrochemical analyses.

2.4. Designing atmospheric chamber and environmental factors

To monitor the atmospheric corrosion occurrences during droplet shape evolution, we have designed a homemade atmospheric corrosion setup (Fig. 2**d**) to perform the electrochemical measurements under single droplets using the wire electrodes. This enabled us to execute precise measurements with good control of the electrolyte volume and height. Also, all electrochemical analyses were performed inside the simulated atmospheric chamber to monitor temperature and relative humidity (RH, EasyLog, EL-USB-2) during droplet shape evolution. All electrochemical measurements were performed inside our chamber under the following environmental conditions: temperature ~21 °C, dew point ~12 °C and relative humidity (RH) ~52 %. An overview of parameter values measured during experiments, as well as their standard deviations, are reported in Figs. 2**b and** 2**c**. Moreover, a humidifier

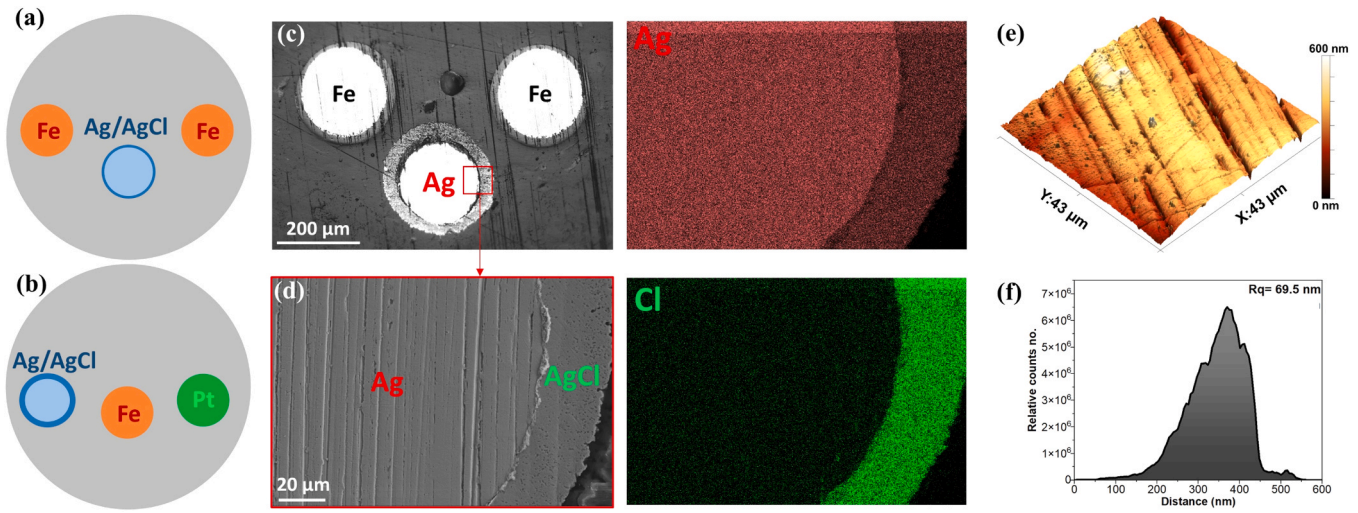

Fig. 1. A schematic demonstration of our designed electrodes for (a) EN and (b) PDP and EIS analyses, (c) A macrograph image of two Fe wires plus Ag/AgCl electrode mounted in cold epoxy resin for EN measurement, (d) A SEM image of Ag-core and AgCl-shell interface to distinguish the individual regions plus corresponding EDXS elemental maps, (e,f) Topography map and corresponding histogram of Fe fresh surface, respectively.

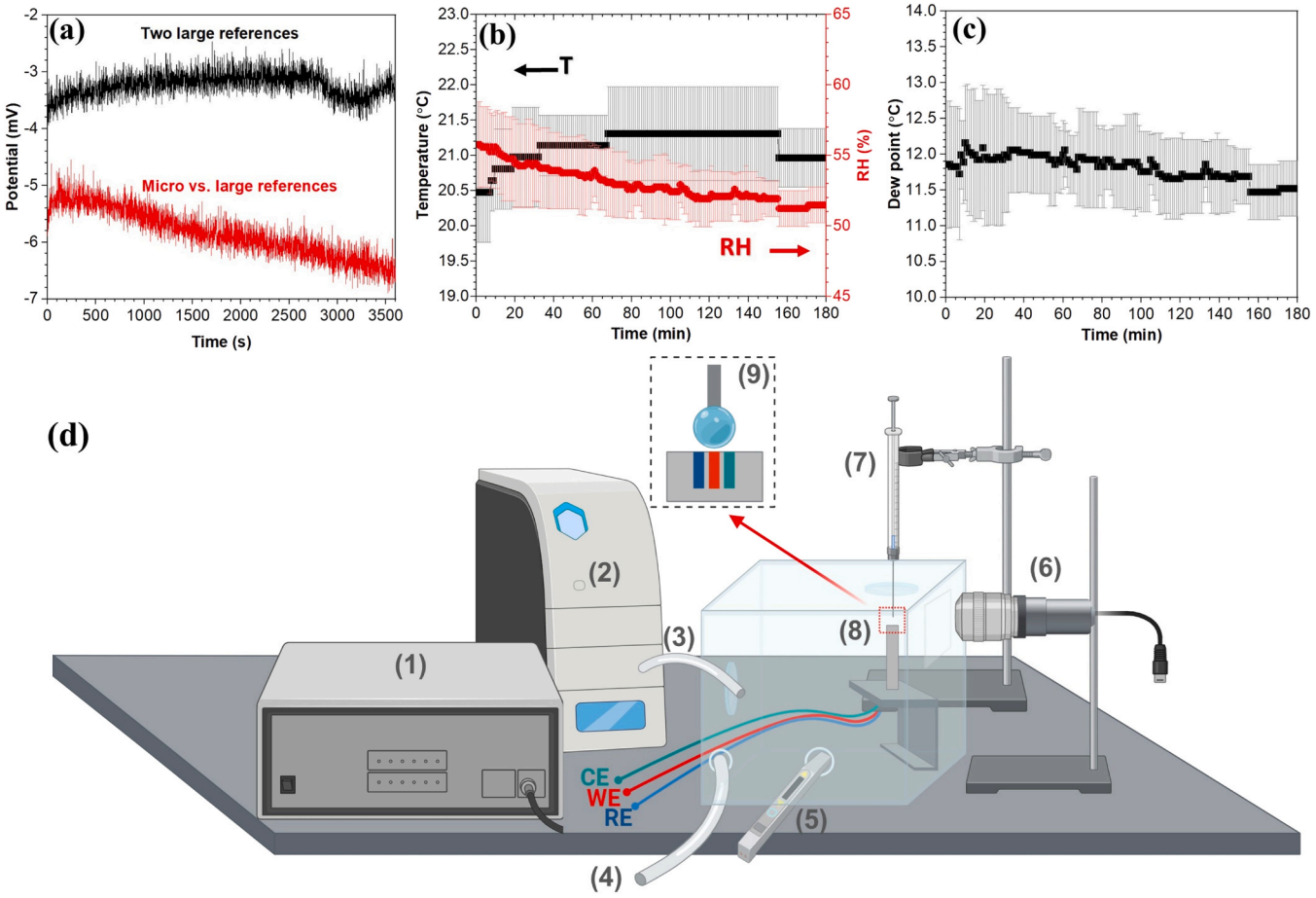

Fig. 2. (a) Potential difference vs. time monitoring in two conventional large-scale Ag/AgCl reference electrodes (black line); designed micro-scale and conventional large-scale reference electrodes (red line). The average values of (b) RH and temperature along with (c) dew point during our atmospheric corrosion measurements inside the chamber, (d) schematic representation of our homemade atmospheric setup including (1) potentiostat, (2) humidifier, (3,4) inlet and outlet pipes of humidifier, (5) temperature and humidity sensor, (6) camera, (7) syringe, (8) top surface of micro-sized three-electrode cell, (9) zoom-in on the top surface of micro-sized electrodes (8), three colors are assigned to Fe (red), Ag/AgCl (dark blue), Pt (green), note: for electrochemical noise analysis, Pt has been replaced by Fe.

(AH660 Medisana) and a laboratory syringe (500 μL, 1750TPLT, Hamilton) were used to control the humidity inside the chamber and to place the single droplets with precise volume/height on the wire electrodes, respectively. Since the injected single droplet with various sizes and NaCl concentrations gradually evaporates, both alterations in droplet shape and evolutions in surface morphology of pure iron (e.g. corrosion products) need to be monitored by a camera (DMK 33UX250, Monochrome- 2448×2048 (5 MP), The Imaging Source) and optical microscope (5x magnification), respectively.

2.5. Electrochemical noise (EN) measurement and analysis

The electrochemical current and potential noise (ECN and EPN) signals of the pure iron surface (EN configuration in Fig. 1**a**) under the single droplets were analyzed simultaneously by an Ivium compact potentiostat operating in EN mode (ASTM-G199). The noise resistance was calculated as the standard deviation of EPN divided by the standard deviation of ECN: $R_n = \sigma_{EPN}/\sigma_{ECN}$. All EN analyses were performed at least three times under open circuit potential (OCP) in the Faradic cage to avoid interference from external electromagnetic sources. The EN measurements were conducted over a period of 1800s at a sampling frequency of 5 Hz using a low-pass filter of 10 Hz.

To reveal further information regarding the type of corrosion processes, the continuous wavelet transform (CWT) spectrum was applied to all ECN signals to extract the time-frequency information utilizing the Morlet wavelet analysis [29,30]. Additionally, an eight-level discrete wavelet transform (DWT) with a Daubechies 4 wavelet was applied for time-frequency trend removal (Supporting information, Figure S1). After this trend removal filtering process, the energy distribution plot was considered to disclose the relative energy caused by each crystal (EN signal at several time scales or resolutions in so-called crystals) to the total ECN signal [31]. The results are presented as relative energy distribution versus detail crystals D1 to D8. From prior studies [29,31], employing these 8 crystals (i.e. an 8-level decomposition) can provide sufficiently detailed information regarding the electrochemical signals and corrosion processes.

2.6. PDP and EIS measurements

The cathodic potentiodynamic polarization (PDP) was performed after 5 min OCP monitoring of the pure Fe surface, from +50 mV vs. OCP to −1.2 V vs. Ag/AgCl. The EIS measurements were conducted in the frequency range from 100 kHz to 0.1 Hz by applying a ±10 mV sinusoidal excitation signal by a Biologic SP 300 multichannel potentiostat for a duration of 2.5 min for each measurement. All EIS and EN measurements were carried out during the gradual evaporation of a single droplet as dynamic electrochemical monitoring until the 1800s. The fitting process of all EIS data was conducted using the most accurate equivalent electrical circuits (EEC) in the Zview software (Supporting information**,** Table S1) and employing relevant previous investigations [32–36]. Both PDP and EIS analyses were recorded in a micro-sized three-electrode cell at Fe/Ag-AgCl/Pt configuration (Fig. 1**b**). All electrochemical analyses including PDP, EIS, and EN were repeated at least three times.

3. Results and discussion

3.1. Geometry evolution of single droplets with different sizes and NaCl concentration

Under realistic atmospheric conditions, any single water droplet (e.g. cold or warm, polluted, soil droplet, etc., [37–39]) formed on metallic surfaces is prone to evaporation or condensation in the initial stage of atmospheric corrosion, as a dynamic electrochemical-shape evolution process. Therefore, monitoring the electrochemical response and particularly the corrosion mechanisms of any kind of metallic surface under a dynamic droplet compared to a stationary droplet will be more representative of a veritable atmospheric corrosion environment. The detailed information on the dynamic evolution of droplet geometry (e.g. shape - hemispherical or spread -, size, etc.) and solution concentration (e.g. alternation in inorganic species) is noteworthy to better understand the corrosion mechanisms [40].

The dynamic shape evolution of single droplets due to the evaporation process was monitored from the initial dropping on the three-electrodes cell until 1800s (Fig. 3). Then, the crucial factors of droplet geometry alongside NaCl concentration were extrapolated from recorded images, as shown in Fig. 4. It is worth mentioning that the curves of both droplet volume (Fig. 4**a**) and surface area (Fig. 4**b**) versus time were determined considering the average of all NaCl concentrations (0.01 M, 0.1 M, and 0.2 M). This is because the exposed surface of the micro-sized three-electrode cell is not an entirely working electrode which is a mixing of RE, CE, and polymer resin (Fig. 1). For this reason, for individual droplet volumes of 5 μL, 3 μL, and 1.5 μL, an average value of all NaCl concentrations was considered. Consequently, the dynamic evolution of these volumes versus time (Fig. 4**a**) was employed to predict the NaCl concentration of droplets over evaporation time, as indicated in Fig. 4**c.** From this figure, it is noticeable that by reducing the droplet volume from 5 μL to 1.5 μL, enhancement on the NaCl concentration (more saturation) shifted from a smooth or linear trend (Fig. 4**c1**) to a semi-logarithmic trendline (Fig. 4**c2 and 4c3**). This behavior is more pronounced at the droplet volumes of 3 μL and 1.5 μL, and both 0.1 M and 0.2 M NaCl concentrations (i.e. red circles and blue triangles in Fig. 4**c2 and 4c3**). Hence, it can be forecasted that the susceptibility of pure Fe to localized corrosion events will be higher in this circumstance due to the higher availability of aggressive Cl^- ions, the more dissolution of Fe, and thus hydrolysis, resulting in a decrease in pH [10,41]. The direct impact of chloride concentration on the acceleration of anodic dissolution and/or localized corrosion of most metals and alloys is well established (iron [6], copper [42,43], aluminum [44], carbon steel [45,46], stainless steel [47]).

3.2. Role of droplet size and NaCl concentration on oxygen reduction reaction

To detect the impact of droplet size and NaCl concentration on the oxygen reduction reaction, a negative overpotential (i.e. cathodic polarization) was applied on a micro-sized Fe electrode. The PDP curves alongside the extrapolated limiting current density (i_{limit}) and corrosion current density (i_{corr}) are shown in Fig. 5. Three distinct regions are visible in the PDP curves, including the mixed control region, limiting current density (mainly oxygen reduction reaction (ORR), Eq. (1)), and hydrogen evolution (Eq. (2)) regions as follows:

$$O_2 + 2H_2O + 4e^- \rightarrow 4OH^- \quad (1)$$

$$2H_2O + 2e^- \rightarrow H_2 \quad + \quad 2OH^- \quad (2)$$

The mixed control region at the beginning of negative overpotential (e.g., cathodic branch) describes that the primary reaction is directed by both electron transfer and mass transport [48]. The plateau region represents the primary reaction under complete mass transport control which is mainly governed by oxygen concentration and its diffusion [49]. The plateau region exhibits the transport of ions, mainly oxygen molecules to the Fe/Fe oxide surface reaching the lowest value than the bulk electrolyte which acts as a determining step (Fig. 5**d**). A meaningful difference is detectable by comparing the approximate onset potential of both limiting current and hydrogen evolution regions in diverse NaCl concentrations (dash lines in Figs. 5**a, 5b, and 5c**). In particular, in 0.01 M NaCl solution, the onset potential starts at −700 mV vs. Ag/AgCl and terminates at −1100 mV vs. Ag/AgCl which is slightly lower than that for both 0.1 M and 0.2 M NaCl (-600 mV to −1050 mV vs. Ag/AgCl), as indicated by dashed lines. It can be attributed to the impact of chloride ions on the solubility of O_2 molecules, ORR, and onset

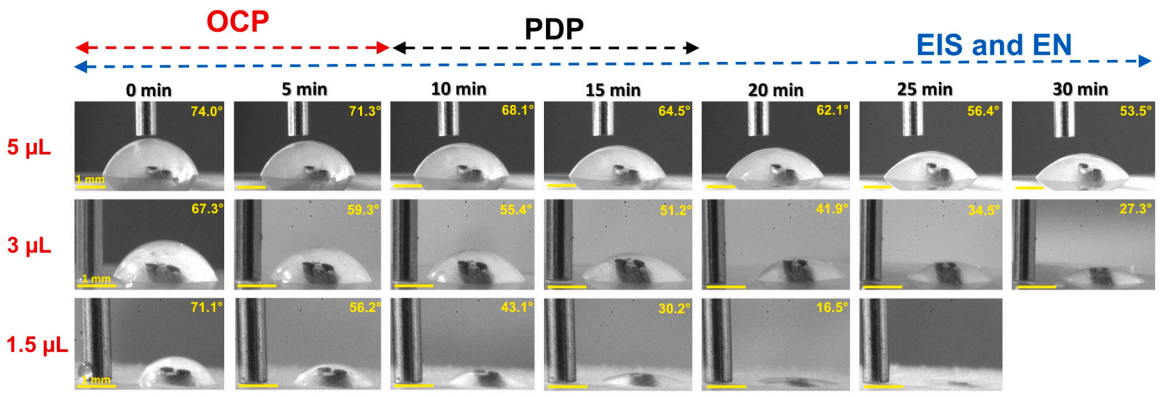

Fig. 3. An example of the macro-photographs for the shape evolution of single saline droplets with various sizes on three electrodes for 1800s. The interval time for capturing images was 5 min.

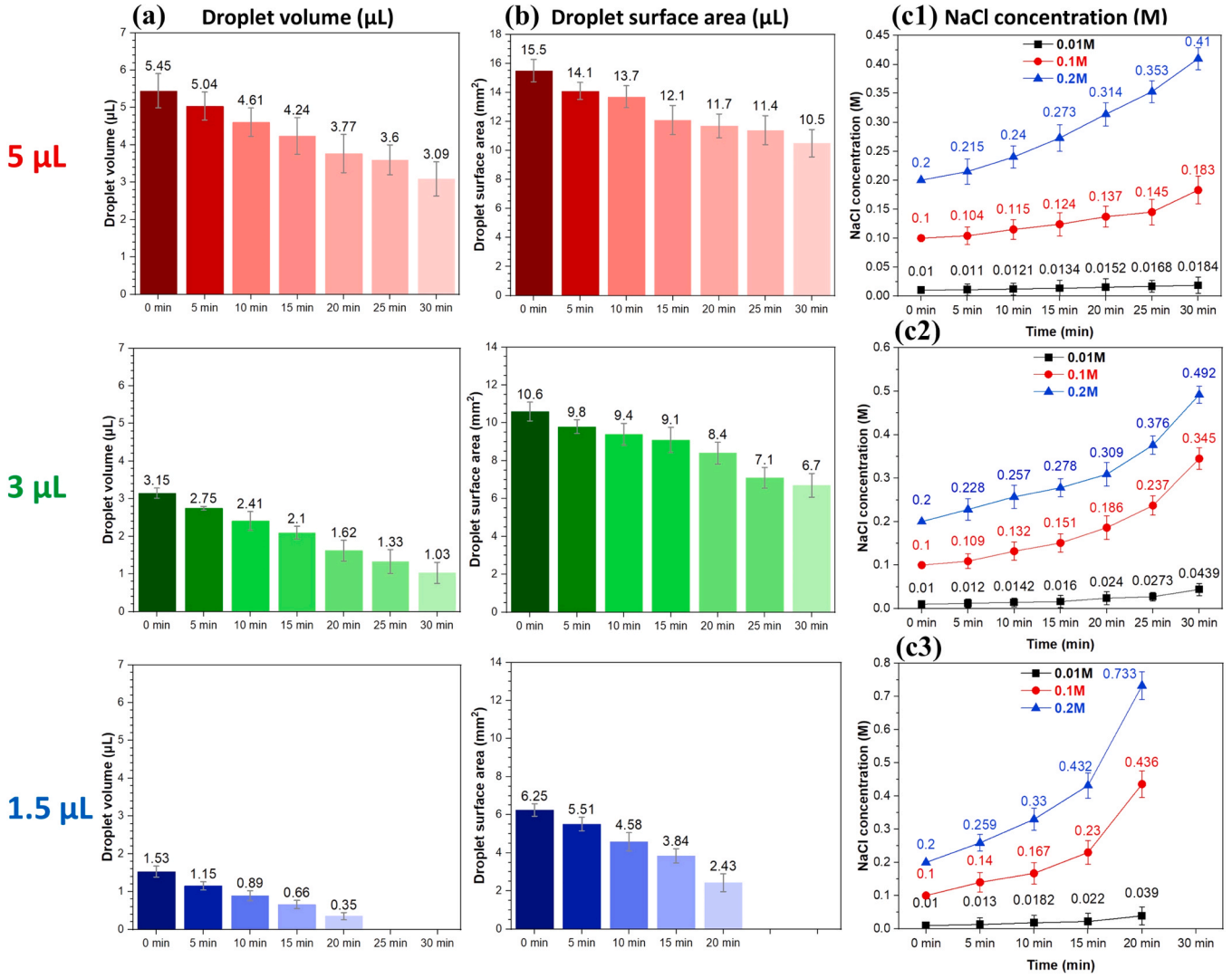

Fig. 4. Droplet volume and NaCl concentration values in single droplets with various initial sizes and NaCl concentrations during the monitoring evolution for1800s (Fig. 3).

potential is predominant. In general, the solubility behavior of O_2 in ionic conductive solution is obscured and chiefly depends on the concentration and composition of dissolved inorganic species. This statement is explained and proposed by Sechenov et al. [50] in the following equation:

$$\log\left(\frac{S^{\circ}_{O_2}}{S_{O_2}}\right) = KC_{Con} \quad (3)$$

Where K is O_2 solubility constant (different for diverse electrolytes), S_{O2}

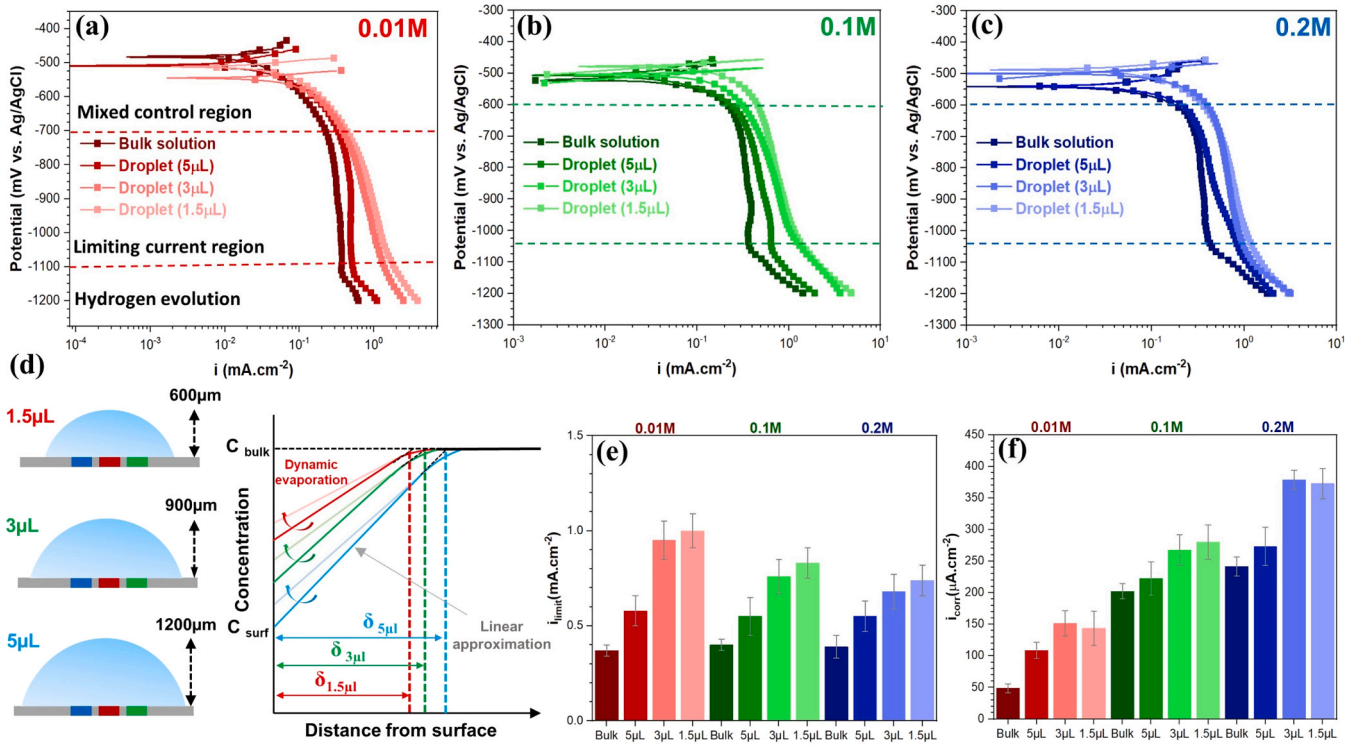

Fig. 5. Cathodic potentiodynamic polarization of pure Fe surface under single droplets with various sizes and NaCl concentrations including (a) 0.01 M, (b) 0.1 M, and (c) 0.2 M NaCl, (d) a schematic representation of the role of droplet size (thickness) on oxygen concentration profile and the thickness of oxygen diffusion layer near to electrode surface with a linear approximation. Extracted electrochemical parameters including (e) limiting current density (i_{limit}) and (f) corrosion current density (i_{corr}) from (a, b, and c).

indicates O_2 solubility in an electrolyte with a concentration (inorganic species) of C_{Con}, S^0_{O2} is O_2 solubility in pure water.

Therefore, by decreasing the inorganic species in the electrolyte (lower C_{Con}), for instance, at 0.01 M NaCl concentration, oxygen solubility increases (higher C_{O2}) due to the less ion-water interaction and fewer void occupations by inorganic species (here Cl^-). This results in an increase in ORR on the cathodic site or applied negative overpotential [50,51]. Consequently, the i_{limit} values at 0.01 M NaCl concentration are higher than 0.1 M and 0.2 M with increasing order 0.01 M > 0.1 M > 0.2 M (Fig. 5**e**), which is more highlighted at 3 μL and 1.5 μL than bulk and 5 μL. The near values of the i_{limit} at bulk and 5 μL volumes in all NaCl concentrations are correlated to the influence of electrolyte volume or thickness on ORR. From Figs. 5**a, 5b, and 5c**, it is evident that by decreasing the droplet volumes from the bulk electrolyte to 1.5 μL in all NaCl concentrations, the plateau region, which is under diffusion control (e.g. limiting diffusion current region) changes to mixed control, with less plateau behavior. This can be explained by Nernst-Fick's Eq. (4) [52] and the schematic illustration in Fig. 5**d**.

$$|i_{Limit}| = \frac{nFDC_{O2,bulk}}{\delta} \quad (4)$$

Where D is the diffusion coefficient, $C_{O2,\ bulk}$ is the concentration of diffusing inorganic species in bulk electrolyte, δ represents the thickness of the diffusion layer (here equal to electrolyte thickness), and F and n are the Faraday constant and the number of transferred electrons, respectively. According to a previous study [7], under a thick electrolyte film (here, 5 μL droplet), a two-dimensional (2D) or spherical diffusion can be considered for ORR (Fig. 6**a**). However, by reducing the droplet volume to 1.5 μL, considering a dynamic evaporation process (Fig. 5**d**), the O_2 diffusion is in a perpendicular direction to the electrode surface, i.e. simple one-dimensional (1D) or planar diffusion (Fig. 6**b**), as described by Eq. (4). Hence, an enhancement in the i_{limit} value alongside a sloped shape of the cathodic branch by reducing the droplet volume or thickness is due to the decreasing δ and less restriction for ORR. In this

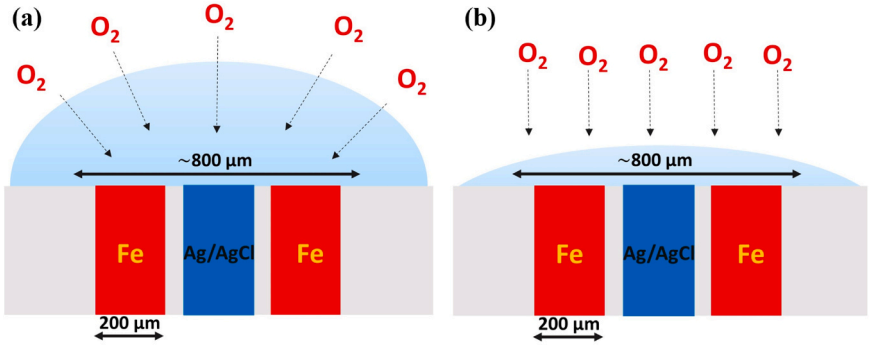

Fig. 6. A schematic representation of (a) two-dimensional and (b) one-dimensional diffusion of oxygen through the hemispherical droplet on our designed micro-sized three-electrodes cell.

circumstance, there is less of a concentration gradient of O_2 between bulk and near metal surfaces as it merely represents a 1D configuration. Please note that the droplet configuration is exposure time-dependent as dynamic evaporation of droplets can cause a dynamic reduction of the electrolyte thickness that affects the value of limiting current density and its geometry, i.e. a 2D diffusion profile may evolve towards a 1D configuration with time (Fig. 3 and Fig. 5**d** schematic profile) [53].

Regarding the impact of droplet volume and chloride concentration on corrosion current density, a dual behavior can be discerned from PDP curves and extrapolated i_{corr}. Reducing the droplet volume from 5 μL to 1.5 μL, the value of i_{corr} gradually increased, particularly at low droplet volume (3 μL and 1.5 μL). As aforementioned, at low droplet volume and considering the dynamic evaporation process, a higher concentration of O_2 molecules will be available to participate in ORR at the Fe surface under one-dimensional diffusion and mixed control. Conversely, it is established that chloride ions play a crucial role in accelerating the dissolution process of metals and alloys since the chemical affinity of the metallic surface for chloride ions is greater than the O_2 molecules. This results in higher annihilation of the formed oxide layer and promotes active anodic dissolution of metallic substrate [52,54].

3.3. *Monitoring the total polarization resistance of iron in diverse droplet sizes and NaCl concentrations*

The role of chloride concentration on electrochemical response, corrosion resistance behavior, and the type of degradation mechanism of Fe surface was investigated using non-destructive tests as free-exposure tests including EIS and EN (*vide infra*). The EIS analysis was utilized for early-stage monitoring of the electrochemical response, specifically revealing the dynamic corrosion mechanisms of the Fe surface under an

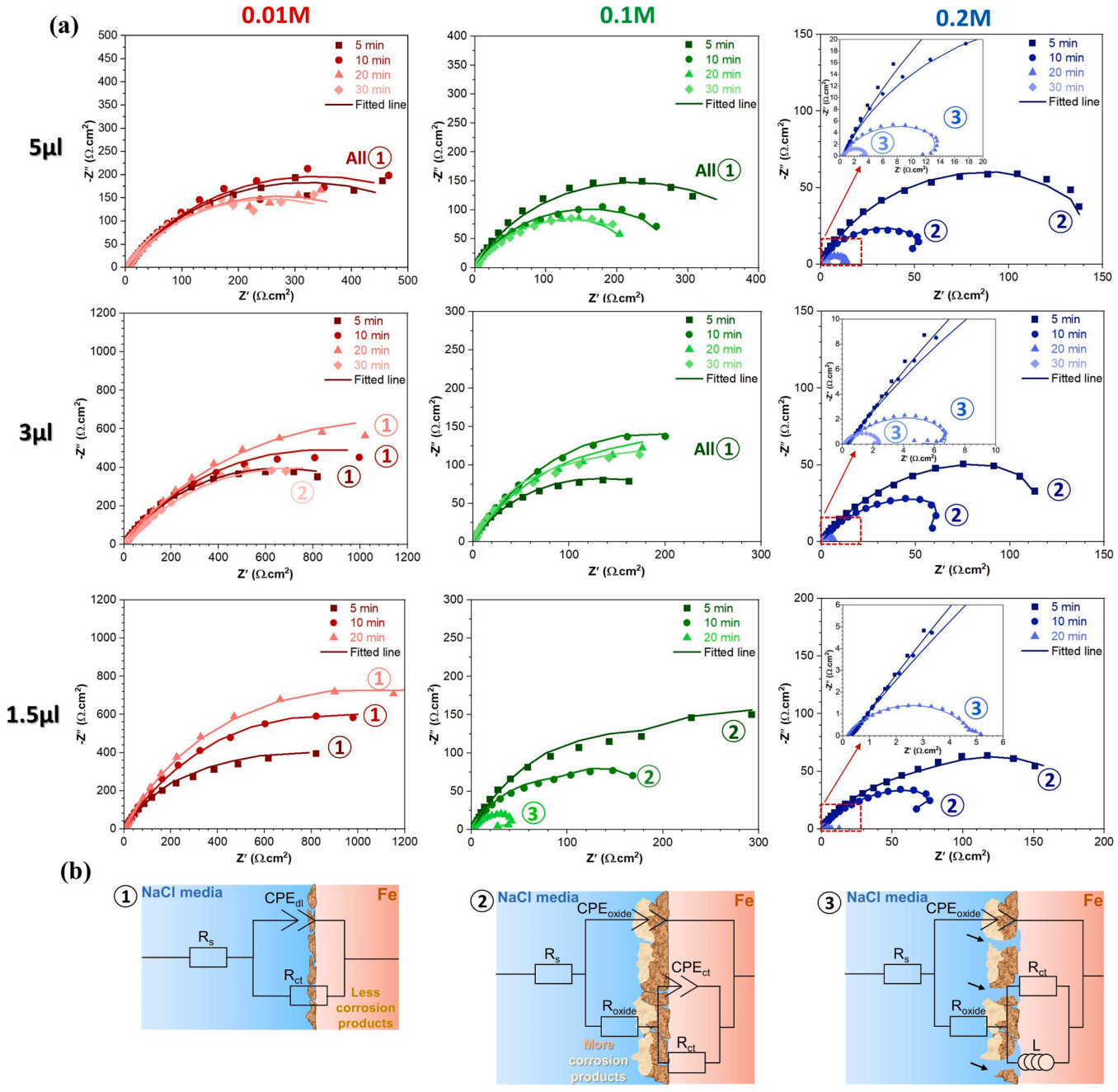

Fig. 7. (a) The Nyquist diagrams of the pure Fe surface under single droplets with various sizes and NaCl concentrations during EIS monitoring until 1800s, (b) The equivalent electrical circuits (EECs) as used in the fitting process of EIS data shown in (a).

evaporating single droplet. The EIS data are presented in Nyquist diagrams in Fig. 7**a** (**Bode diagrams in** Figure S2). Owing to a gradual evaporation process, dynamic AC electrochemical signals or corrosion processes versus time were detected that resulted in different EECs, as presented in Fig. 7**b**. The results of the EIS fitting process are listed in Table S1. Overall, the EEC parameters were detected as follows solution resistance (R_s), charge transfer resistance (R_{ct}), the resistance of the complex oxide layer ($R_{\text{complex oxide}}$), total resistance ($R_t = R_s + R_{ct} + R_{\text{complex oxide}}$), constant phase element of the double layer (CPE_{dl}), constant phase element of the complex oxide layer ($CPE_{\text{complex oxide}}$), and inductor (L). The CPE is utilized instead of a capacitor since the capacitance element has non-ideal behaviour due to both surface heterogeneity and roughness [55].

$$Z_{CPE} = \frac{1}{Y_0 \quad (j\omega)^n} \tag{5}$$

where Y_0 is the admittance of CPE, j is the imaginary unit, ω is the angular frequency, and n is the CPE exponent ($-1 \leq n \leq 1$, −1, 0 and 1 are assigned to a system which is a pure inductor, pure resistance, and pure capacitance, respectively). The simplified Randles circuit was considered in the most fitting process of EIS curves, since their corresponding Nyquist and Bode diagrams almost represent only a sign of single capacitance (e.g. one-time constant), except circuit numbers 2 and 3 (Figure S2 **and** Fig. 7**b**). Hence, according to previous studies [56, 57], it is supposed that the formed rust layer is relatively limited and porous (e.g. low formation of oxide corrosion products such as α or γ-FeOOH and Fe_2O_3 (hematite)[54]) during the early stages of exposure and it could not be accurately distinguished from the metal substrate using EIS analysis (EECs #1 in Fig. 7**b**)[32].

The Nyquist diagram of Fe under the 5 μL, 0.01 M NaCl droplet in Fig. 7**a** exhibits one-time constant during 30 min of monitoring. Additionally, extra relaxation is recognizable in the Bode-phase diagram of Figure S2, in the frequency range of 10–100KHz that can be attributed to solution conductivity alongside the micro-sized reference electrode and dynamic evaporation process. However, for 3 μL and 1.5 μL at 0.01 M NaCl, the extent of this extra relaxation in the Bode-phase diagram is limited and it is entirely absent at high NaCl concentration. Nevertheless, a transition from the one-time constant (simple Randle circuit) to the two-time constants was identified (Fig. 7**a** and EEC in Fig. 7**b**) after 30 min for 3 μL condition that are assigned to individual regions including complex corrosion products and the Fe substrate. From prior investigations, it was revealed that by prolonging the exposure time of the Fe surface, high corrosion products with less porous structure (mainly a combination of α or γ-FeOOH and Fe_2O_3 (hematite)[32]) will be formed that are detectable by EIS analysis [58,59] (*vide infra* in Raman analyses in Fig. 15).

By comparing the total impedance values of the Fe surface under various droplet sizes in 0.01 M NaCl in Fig. 8**a**, a decrement in the R_t value of the Fe surface was visualized at 5 μL during evaporation until 30 min. In contrast, it was enhanced in both 3 μL and 1.5 μL volumes. This occurrence is attributed to the impact of both fewer aggressive Cl^- ions (less anodic dissolution) and dynamic evaporation or thinning of the electrolyte. At 3 μL and 1.5 μL volumes and considering the dynamic evaporation of droplets, a higher concentration of dissolved O_2 molecules will be available to contribute to ORR on the Fe surface under 1D diffusion than 5 μL under a 2D diffusion. Thus, a lower concentration gradient of O_2 molecules or potential distribution between bulk and near metal surfaces can be anticipated (Fig. 6), particularly at low Cl^- ion concentrations that result in a lower corrosion rate. In fact, for small droplet sizes, in particular at high NaCl concentrations, mixed charge transfer (electrons) and mass transport (oxygen, dissolved Fe ions and Cl^-) play a larger controlling role in the kinetics [60]. Simillion et al. [11], using computing modeling, demonstrated that the dynamic evaporation of a thick electrolyte film (500 μm and initial NaCl concentration 0.1 wt%) to a thin film (2 μm) triggers variations in corrosion potential values of zinc surface due to the variation in ORR that displaces equilibrium in anodic and cathodic currents.

By increasing the NaCl concentration to 0.1 M NaCl at 5 μL volume during all evaporation times, only one relaxation process was considered, indicating that the formed Fe corrosion products are non-protective with a porous structure (EEC in Fig. 7**b**) and redox reactions were limited by charge transfer resistance at Fe substrate/electrolyte interface [57,61]. By reducing the droplet size to 3 μL, the EIS fitting process confirmed a one-time constant (a mix condition of thin and porous corrosion product film and Fe substrate [58], EEC in Fig. 7**b**). As the droplet volume decreased to 1.5 μL, two recognizable relaxation processes were noticed in EIS curves during 5 min and 10 min evaporation times. Before reaching a completely dried Fe surface at 20 min, a very small capacitive loop (very low impedance value) alongside an inductive loop at low frequency was monitored. The origin of this inductance loop at low frequencies can be explained by two main opinions: First, the relaxation of adsorbed intermediate products like $FeOH_{ads}$ on the metal surface remarkably influenced this inductance characteristic at low frequencies [35], and second, the non-stationary behavior of most active metallic surface (e.g. Mg [62,63], Al [64,65], and Fe [66]) due to high aggressivity of solution that trigger localized corrosion attacks. The recent work by Wang et al.[36] demonstrated that the non-stationary of Mg-based alloy is a combination of internal non-stationarity and externally induced non-stationarity. Particularly, the internal non-stationarity of Mg-based alloy in various environments is correlated to the growth of a surface oxide film and localized corrosion (in specific Mg-based alloys like AM and AZ series). Owing to a dynamic evaporation process and in turn additional saturation of aggressive Cl^- ions, the tendency of Fe oxide/Fe substrate to high anodic dissolution and localized corrosion event is enhanced as proved by the most suitable EEC (Fig. 7**b**) and prior investigations [33,67]. This is consistent with localized corrosion attacks observed in optical microstructural images (*vide infra* in Fig. 14**a**) acquired after the electrochemical noise analysis

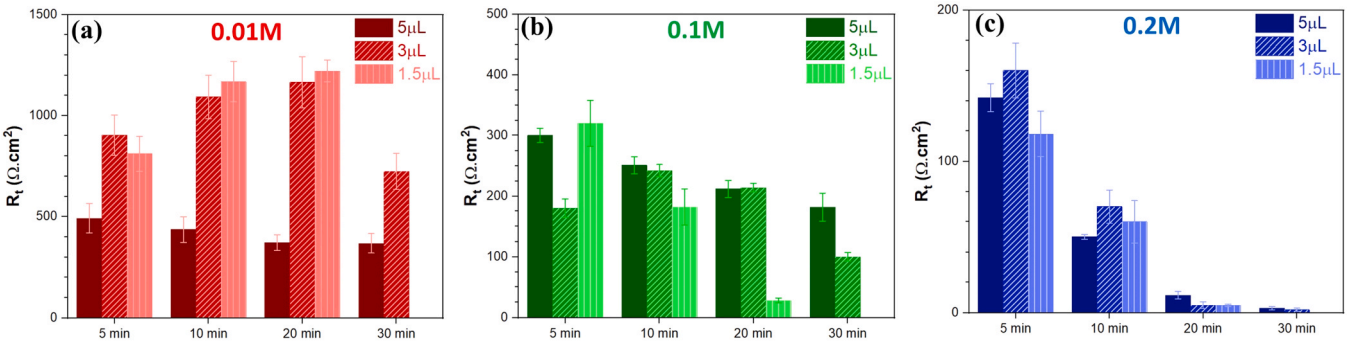

Fig. 8. Early-stage monitoring (interval time was 5, 10, 20, and 30 minutes after injection) on total resistance (R_t) values (at 0.1 Hz) of pure Fe under various droplet sizes and NaCl concentrations, including (a) 0.01 M, (b) 0.1 M, and (c) 0.2 M.

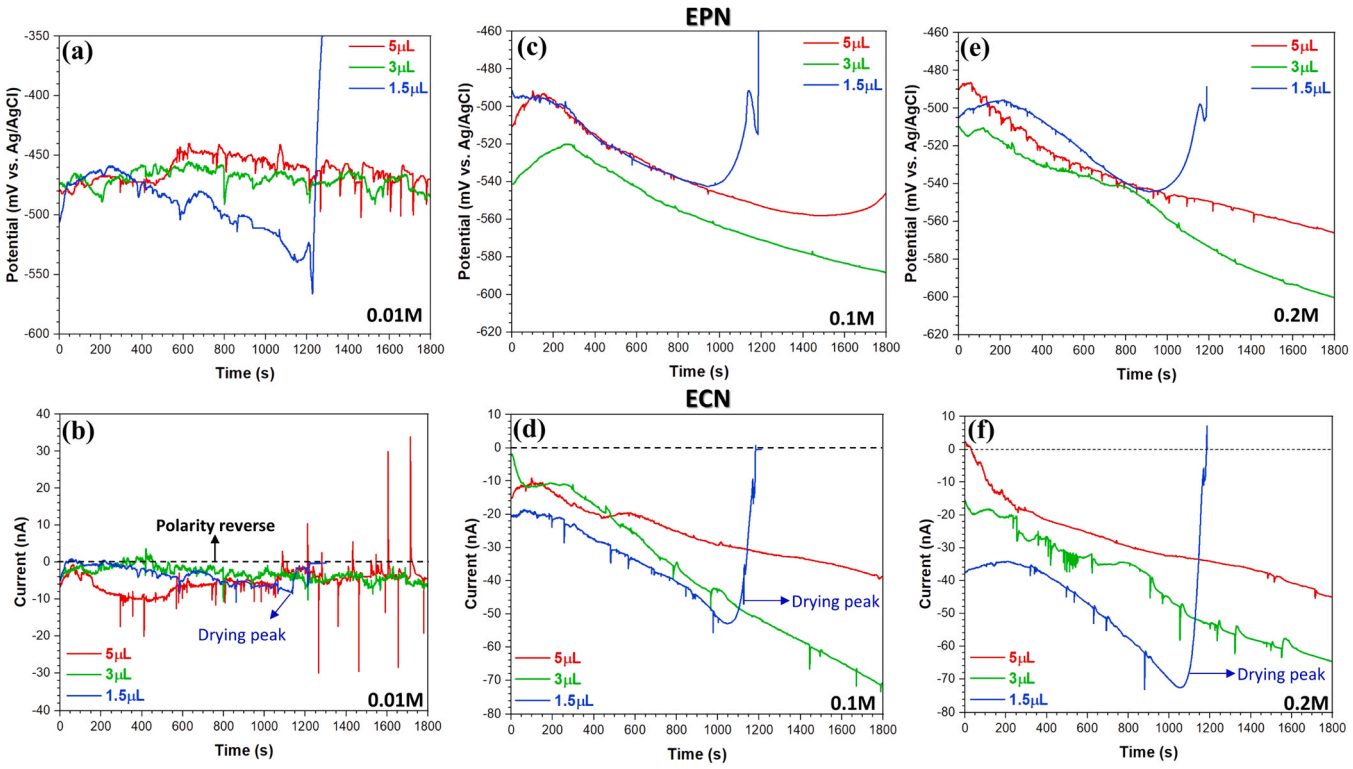

Fig. 9. EPN and ECN curves of pure Fe electrodes under various droplet sizes and NaCl concentrations including (a,b) 0.01 M NaCl, (c,f) 0.1 M NaCl, and (e,f) 0.2 M NaCl.

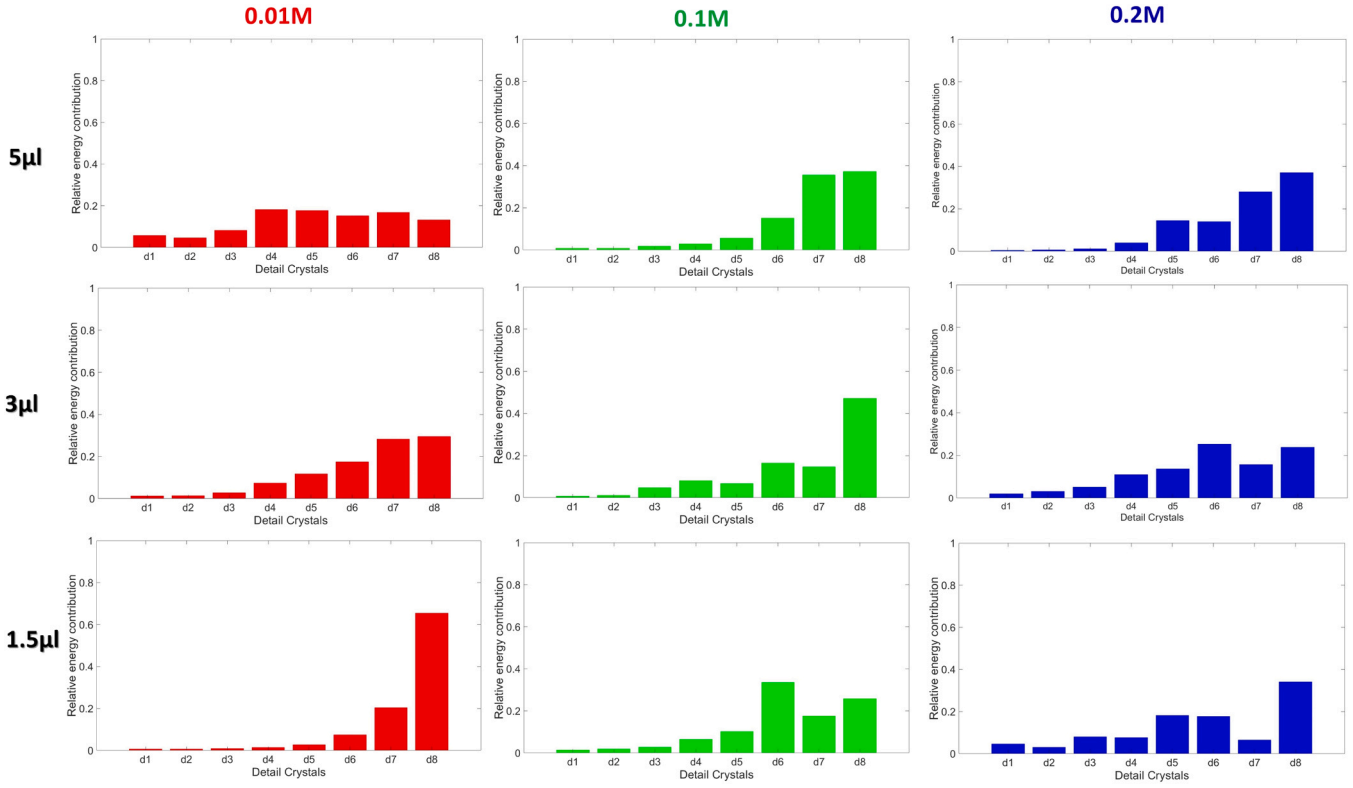

Fig. 10. Energy distribution plots (DWT) of the ECN signals of pure Fe electrodes under various droplet sizes and NaCl concentrations.

(which will be discussed in full detail information in the next section).

The total impedance values of the Fe surface in 0.1 M NaCl and all droplet sizes in Fig. 8**b** demonstrate a decreasing trend of R_t value during the dynamic evaporation which confirms the pivotal impact of aggressive Cl^- ions on Fe dissolution and chemical instability of formed semi-protective corrosion products (e.g. Fe_2O_3). This destructive

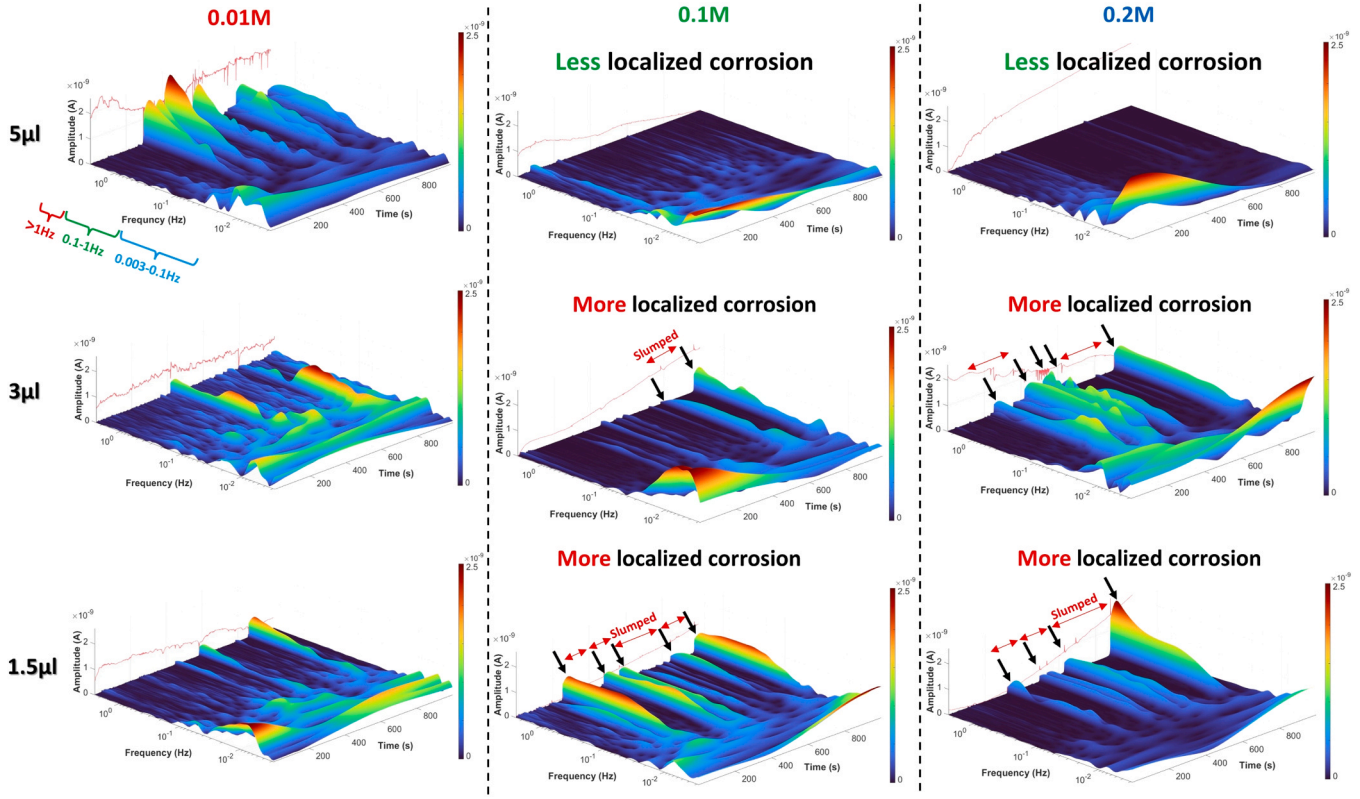

Fig. 11. CWT spectra of all ECN signals as shown in Fig. 9.

phenomenon is highlighted at 0.2 M NaCl since all droplet volumes at the beginning (e.g. 5 min and 10 min) indicate two relaxation processes that evolve to extremely small capacitance loop (very low impedance value) at 20 min and 30 min along with an inductive loop at low frequency (Fig. 7**a**). According to previous studies on carbon steel [68], tin [69], and aluminum alloys [70], the presence of an induction loop at low frequencies is assigned to the formation of pits at defective sites due to the adsorption of aggressive Cl^- ions in a active region that further accelerate local metal dissolution. This two-times increase in NaCl concentration from 0.1 M to 0.2 M further establishes the predominant role of aggressive Cl^- ions in accelerating the anodic dissolution of a pure Fe surface in the form of localized corrosion that remarkably reduced the total impedance during dynamic evaporation (Fig. 8). Consequently, the appearance of the inductance loop at low frequency and in high NaCl concentration can be ascribed to three combined (even simultaneous) events: dynamic saturation of Cl^-, adsorption/desorption of intermediate species, and internal non-stationarities induced by the localized corrosion process and/or external non-stationarities introduced by EIS analysis [36]. In the EN section, it is intended to explore the correlation between the magnitude of EIS impedance and the noise resistance (R_n) and non-stationary observations obtained from EN data during the dynamic evaporation process until 30 min.

3.4. Monitoring the current and potential noise signals of Fe in diverse droplet sizes and NaCl concentrations

The EPN and ECN signals revealed the early-stage electrochemical activity of the Fe surface under the single droplets. As presented in Fig. 9**b,** it is observed that in a 0.01 M NaCl solution and with 5 µL droplet volume, the Fe surface displayed a substantial magnitude of the ECN signal, including larger fluctuations (and hence a larger standard deviation σ_{ECN}) as compared to the other droplet volumes (3 µL and 1.5 µL). These large current oscillations are visualized in more detail by employing a discrete wavelet transform (DWT) to the ECN signals, which is visualized in Fig. 10**.** Here, an energy distribution plot is shown, ranging from the relative energy contribution in the signal at the smallest timescale detail crystal D1 to the largest timescale D8. At 5 µL droplet volume, detail crystals D4 and D5 contain a relatively large amount of energy, proving the heterogeneity of the system under mixed control, with additionally a slightly increased contribution of the smallest timescales reflected in detail crystals D1-D3 [31].

This kind of electrochemical response with high-frequency fluctuations in the EN analysis can be ascribed to mainly localized corrosion processes [30]. However, by decreasing the droplet size from 5 µL to 1.5 µL, an inverse process was observed in which the ECN magnitude and fluctuations diminished and gradually reached zero (polarity reverse line). Additionally, the relative energy distribution of detail crystals D1-D6 gradually diminished, whereas D7 and D8 increased, which corresponds to a smoother ECN signal that, combined with the decrease of the average value of the ECN, is an indication of reduced electrochemical activity at the Fe surface [31]. Particularly, the ECN signal of the Fe surface under the 1.5 µL droplet eventually reaches zero after a rise of the current peak at ~1200 s, confirming that the droplet completely evaporated (blue arrow as drying peak in Fig. 9**b**). This corresponds well with the optical macrograph shown in Fig. 3,

Fig. 11 presents the kinetics of all electrochemical interactions in detail in the time-frequency domain. As shown in the spectra at 0.01 M NaCl, the energy distribution, including the relatively large red spikes at high frequencies, as marked by “High” (>1 Hz), reduces (less electrochemical activity) with reducing droplet volume. Under the same surface area that is covered by various droplet sizes, decreasing the droplet volume or thickness generates a shorter diffusion path for O_2 molecules to reach the Fe surface. Therefore, at 1.5 µL volume, a lower oxygen concentration gradient around the Fe surface for the ORR will be established (or less driving force for the oxygen concentration cell), thus causing a more homogeneous distribution of the corrosion potential at the lowest Cl^- concentration (there is less anodic dissolution as well) [14]. Hence, the uniform corrosion process which is accompanied by

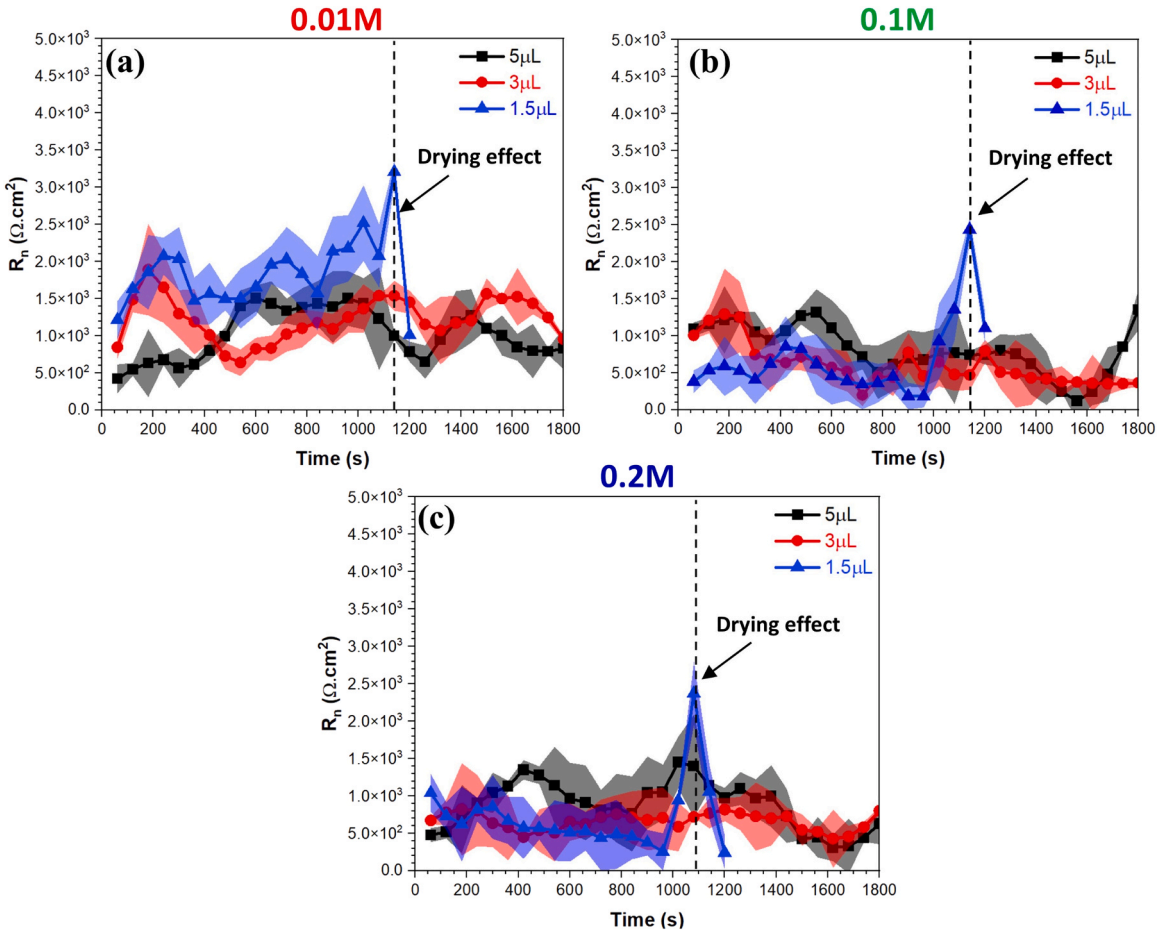

Fig. 12. R_n vs. time monitoring of a pure Fe surface under a single droplet with various sizes and NaCl concentrations ((a) 0.01 M, (b) 0.1 M, and (c) 0.2 M) during EN monitoring until 1800s. Note: in the case of a single droplet with a volume of 1.5 μL, the total measurement duration was ~1200 s.

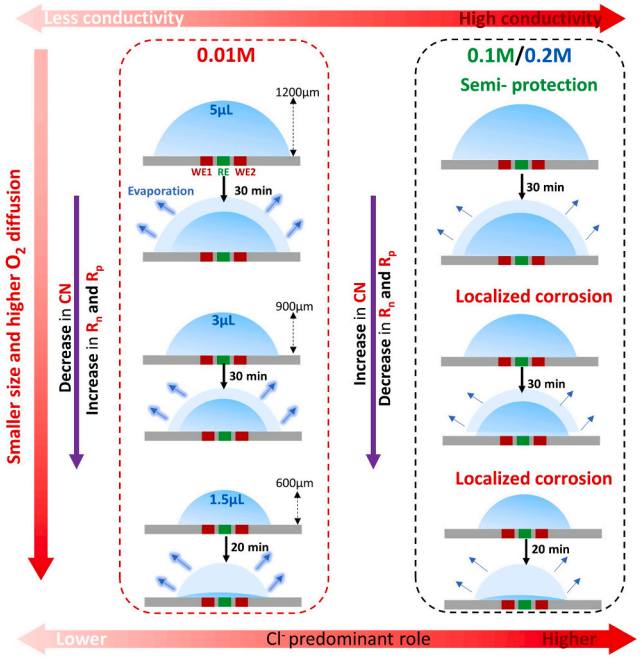

Fig. 13. Schematic representation of the physicochemical and electrochemical response of a pure Fe surface under a single droplet as a function of size and NaCl concentration under atmospheric exposure conditions.

localized events (associated with relatively high current spikes in medium- (0.1–1 Hz) and high frequencies (>1 Hz)) in the early rust layer (mostly γ-FeOOH [57]) reduces with decreasing droplet volumes. This is consistent with the increase in total impedance value achieved from both EIS data (**Figure 8)** and R_n (Fig. 12**)** alongside a decrease in Fe corrosion product formation, visible in the optical micrograph in Fig. 14**a**. Additionally, according to prior studies [57,71], the infrequent, large fluctuations in the ECN or in the CWT spectrum at 0.01 M NaCl can be attributed to the instability of an early-formed film of corrosion products such as soluble ferrous hydroxide ($Fe(OH)_2$) or accumulated γ-FeOOH that contain cracks and may partially dissolve, facilitating O_2 molecules and Cl^- ions to reach the metal surface.

Upon increasing the NaCl concentrations from 0.01 M to 0.1 M and then 0.2 M at constant large droplet size (5 μL), Figs. 9**d and** 9**f** show an increasingly intensive ECN without significant current fluctuations or distinctive peaks, at NaCl concentrations of 0.1 M and 0.2 M. This is further evidenced by the DWT representation in Fig. 10, in which a lower energy contribution can be visualized in D1-D3. However, the energy contribution gradually increases towards D8, demonstrating a relatively smooth ECN. Analyzing the CWT spectrum in Fig. 11, two phenomena could be distinguished from the ECN signal. These include an intensive energy peak (dominant red peak) for 0.2 M NaCl at "Low" frequencies (3 mHz to 0.1 Hz), probably due to intensive uniform corrosion, and peaks at "High" and "Medium" frequencies for 0.01 M NaCl that can be assigned to the formation of corrosion products with semi-protective behavior leading to localized attack, respectively [30, 72]. As a statistical parameter, the value of R_n is inversely proportional to the corrosion rate (for example, corrosion current density). Figs. 12**b**

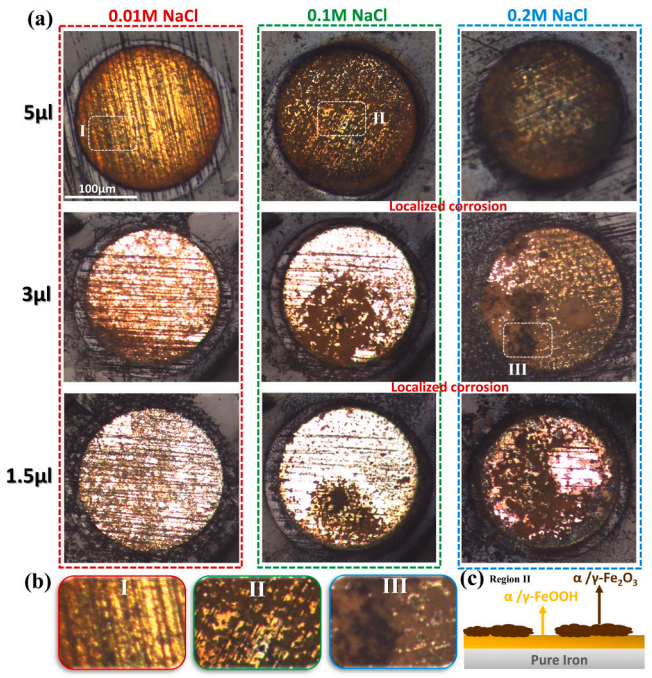

Fig. 14. (a) Optical microscopy images of pure Fe surfaces in electrochemical noise configurations under single droplets with various NaCl concentrations (0.01 M, 0.1 M, and 0.2 M) and three different volumes (5 µL, 3 µL, and 1.5 µL) after 1800s of exposure, (b) Zoomed-in images of regions I, II, and II, (c) A schematic representation of Fe corrosion products distribution at 5 µL and 0.01 M NaCl (zoomed-in image at region II). The image of all electrodes, including working electrodes #1 and #2, and reference electrodes, are presented in Fig. S3.

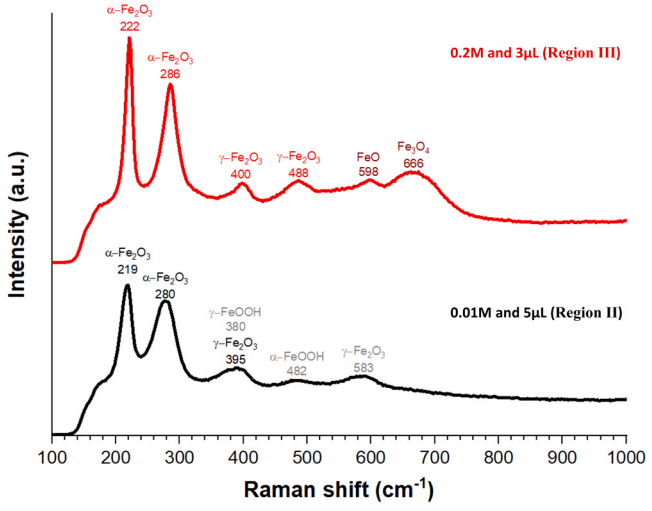

Fig. 15. The Raman spectra of the Fe corroded surface after EN monitoring until 1800s.

and 12**c** exhibit an overall decrease in the R_n value of the Fe surface in both 0.1 M and 0.2 M NaCl concentrations over decreasing droplet size which is consistent with EIS data (Fig. 7**a and** Fig. 8) and the extracted i_{corr} from the PDP analysis in Fig. 5**f**.

Nevertheless, by decreasing the droplet size from 5 µL to 1.5 µL at both 0.1 M and 0.2 M NaCl (Figs. 9**d and** 9**f**), the magnitude of the ECN value intensively increased alongside the appearance of new current peaks that can be ascribed to localized corrosion attack, which are mainly metastable events (e.g. rapid rise continued by exponential decline [72]), as shown in the optical micrograph in Fig. 14**a**. Furthermore, this is proven by the DWT (Fig. 10) that shows an increase in the energy distribution at medium detail crystals (D4-D6) and a decrease for detail crystals D7 and D8. Additionally, for 0.2 M also the energy distribution in D1-D3 increases gradually with decreasing droplet volume. Similar to the DWT, some continuous (expanded red and light green color peaks) ECN peaks in Fig. 11 become evident mainly at "Mid-high" frequencies (from 20 mHz to 2 Hz). Each transient quickly decreases back to the matrix current distribution (red and black arrows in Fig. 11). This further proves the initiation and quick repassivation of metastable events (which corresponds to a large amount of corrosion products with semi-protective action in this case). It is worth mentioning that the baseline currents in Figs. 9**d and** 9**f** and their corresponding CWT spectra ("Low" frequencies (3 mHz to 0.1 Hz)) represent an intensive uniform corrosion process and, as a result, the formation of large amounts of corrosion products. Since there is a dynamic evaporation process and a higher saturation of Cl^- ions, the baseline ECN (uniform corrosion process) will increase over time, which triggers a steep trend rather than the formation of a plateau (Figs. 9**d and** 9**f**). Finally, Fig. 13 schematically depicts the impact of droplet size and NaCl concentration on the corrosion processes of the Fe surface during dynamic evaporation.

3.5. *Characterization of corrosion products under various droplet sizes and NaCl concentrations*

Fig. 14**a** represents a surface micrograph image of the Fe surface after EN measurement during the 1800s under all droplet sizes and NaCl concentrations. Generally, by the formation of a thin film electrolyte, atmospheric corrosion will proceed by balancing the anodic dissolution of Fe and the reduction reaction which is assumed to be the O_2 reduction reaction (Eq. 1). The first diffusion barrier layer that forms on the Fe surface is ferrous hydroxide $Fe(OH)_2$ due to the interaction of OH^- with Fe^{2+} ascribed as follows [71]:

$$Fe^{2+} + \frac{1}{2}\ O_2\ (g) + \ H_2O \rightarrow \ Fe(OH)_2 \qquad (6)$$

The $Fe(OH)_2$ corrosion products are soluble in the electrolyte causing to formation of passive films that directly affect the overall rate of anodic dissolution of the Fe surface. The continuous interaction of the $Fe(OH)_2$ with more O_2 and water molecules forms $Fe(OH)_3$, as follows [71]:

$$2Fe(OH)_2 + \frac{1}{2}\ O_2\ (g) + \ H_2O \rightarrow \ 2Fe(OH)_3 \qquad (7)$$

Due to highly accessible dissolved O_2, the ferrous oxide ($Fe(OH)_2$) converts to ferric hydroxide (FeOOH) according to the following reaction:

$$2Fe(OH)_2 + \frac{1}{2}\ O_2\ (g) \rightarrow \ 2FeOOH + \ H_2O \qquad (8)$$

Since the FeOOH is unstable, it will transform into the new stable stoichiometry state of Fe oxides, which are the most common verities of Fe oxides, including goethite (α-FeOOH) and lepidocrocite (γ-FeOOH). These types of Fe corrosion products or rusts (formerly observed [73, 74]) can be formed at 5 µL and 0.01 M NaCl conditions (Fig. 14**a**, **region I** zoomed-in at the bottom, Fig. 14**b**). However, by decreasing the droplet size from 5 µL to 1.5 µL, the amount of the corrosion products is reduced and their presence becomes scattered, limiting the possible protection effect. Nonetheless, by increasing the NaCl concentration to 0.1 M and 0.2 M at 5 µL, the reddish brown and/or brown color corrosion products (marked as **region II**) formed on the matrix with the same color distribution at 5 µL and 0.01 M NaCl. According to the Raman spectrum analysis in region II (Fig. 15), it is assigned to the formation of hematite (α-Fe_2O_3) and maghemite (γ-Fe_2O_3) that deposited on the yellow and reddish-orange colored corrosion products as a matrix (these are related to α-FeOOH and γ-FeOOH, see peaks in Fig. 15). This is

schematically indicated in the right-bottom in Fig. 14**c**. In 0.2 M NaCl solution compared to 0.1 M NaCl at 5 μL, there is a noticeable increase in corrosion rate and iron dissolution (increased rust formation is evident in Fig. 14), indicated by a higher i_{corr} and ECN amplitude, as well as a lower R_t and R_p in both DC and AC electrochemical evaluations [75,76].

A heterogeneous distribution of reddish-brown to dark brown corrosion products is observed when the droplet size is reduced from 5 μL to 1.5 μL in both 0.1 M and 0.2 M NaCl concentrations. At 3 μL and 1.5 μL, 0.2 M NaCl, the electrode surface exhibits an increased corrosion product formation as well as increased signs of localized corrosion attack as compared to 0.1 M NaCl (Fig. 14). This observation aligns with energy distribution plots (DWT), which show increased detail crystal D1-D4 for 0.2 M NaCl.The random Raman spectra analysis of the sample at 0.2 M and 3 μL (**region III**) indicates the formation of the magnetite (Fe_3O_4) and FeO plus of α-Fe_2O_3 and maghemite γ-Fe_2O_3. At high NaCl concentration and small droplet size, the γ-FeOOH accumulates on the Fe metallic surface and forms the early outer rust layer which acts as a pseudo-barrier layer for surpassing the chloride ions diffusion. Because of the electrical contacting of γ-FeOOH thin film with the metallic substrate, the following reduction reaction also could occur as follows [57]:

$$3\gamma - FeOOH + H^+ + e^- \rightarrow \quad Fe_3O_4 + \quad 2H_2O \tag{9}$$

According to a previous study utilizing IR spectroscopy [57], it was proved that Fe_3O_4 can be formed directly from other Fe corrosion products, especially in high NaCl concentrations (3 % NaCl). This is not only a reason for the localized corrosion attacks at high NaCl concentrations (0.1 M and 0.2 M NaCl) and low droplet sizes (3 μL and 1.5 μL) observed by EIS (significant decrease of impedance value and appearance of inductance loop) and EN (intensive background current with multiple transient peaks (metastable events)) but also for establishing the formation of Fe_3O_4 and FeO that mainly appeared near the localized attack sites [54].

4. Conclusions

A systematic multi-electrochemical approach was considered for the early-stage monitoring of the electrochemical properties and corrosion processes of pure Fe under various single droplets with different volumes and NaCl concentrations. The key findings are summarized as follows:

1. By reducing the droplet size from 5 μL to 1.5 μL at all NaCl concentrations, an increase in i_{limit} alongside a switching from diffusion- to mixed control (increased localized activity) was observed. The slope of the cathodic polarization branch changed from a plateau with a relatively low ORR to a slope with a higher ORR due more access of O_2 for the ORR and a lower O_2 concentration gradient. This was due to the change from a two-dimensional (2D, 5 μL) to a simple one-dimensional (1D) O_2 diffusion process at 1.5 μL, which caused a high level and uniform distribution of O_2 at the Fe surface.
2. By increasing the NaCl concentration from 0.01 M to 0.2 M, the Fe surface under various droplet sizes represented a decreasing trend in i_{limit} and an increase of i_{corr}, indicating: i) that a high concentration of Cl^- ions remarkably decreases the diffusion of O_2 and decreases its mobility processes and ii) its large impact on the anodic dissolution of the Fe surface.
3. At 0.01 M concentration and 5 μL droplet volume, the Fe surface generated a high magnitude of ECN and fluctuations (large σ_{ECN}) until 1800s. Nonetheless, by reducing the droplet size from 5 μL to 1.5 μL at the same concentration, an inverse process was observed in which the ECN magnitude and fluctuations diminished, leading to an increase in R_n as well as R_p.
4. By increasing the NaCl concentrations from 0.01 M to 0.1 M and then 0.2 M at 5 μL droplet volume, an increase in the magnitude of the ECN baseline magnitude was detected with a relatively smooth current noise, that could be ascribed to active uniform corrosion. However, by reducing the droplet size from 5 μL to 1.5 μL, the magnitude of the ECN fluctuations significantly increased due to localized corrosion events, resulting in a decrease of R_n and R_p.
5. The combined DC and AC electrochemical analyses noticeably infer that rather than oxygen diffusion, Cl^- ions represent the rate-determining step at high NaCl concentrations (0.1 M and 0.2 M) By contrast, at low NaCl concentration (0.01 M), the role of O_2 molecules is predominant.

CRediT authorship contribution statement

Ehsan Rahimi: Writing – review & editing, Writing – original draft, Methodology, Formal analysis, Data curation, Conceptualization. **Axel Homborg:** Writing – review & editing, Formal analysis, Data curation. **Nils Van den Steen:** Writing – review & editing, Data curation. **Ali Kosari:** Methodology, Formal analysis, Data curation. **Keer Zhang:** Writing – review & editing, Data curation. **Herman Terryn:** Writing – review & editing, Investigation, Formal analysis, Data curation. **Yaiza Gonzalez-Garcia:** Writing – review & editing, Supervision, Resources, Funding acquisition, Conceptualization. **Arjan Mol:** Writing – review & editing, Supervision, Conceptualization.

Declaration of Competing Interest

The authors declare that they have no known competing financial interests or personal relationships that could have appeared to influence the work reported in this paper.

Data Availability

Data will be made available on request.

Acknowledgments

This research was carried out under Project no. T18016 in the framework of the Research Program of the Materials Innovation Institute (M2i) supported by the Dutch Government. The authors also acknowledge Roald van der Kolk (Kavli Institute of Nanoscience, Delft University of Technology) for performing the Raman analysis.

Appendix A. Supporting information

Supplementary data associated with this article can be found in the online version at doi:10.1016/j.corsci.2024.112171.

References

[1] R. Bender, D. Féron, D. Mills, S. Ritter, R. Bäßler, D. Bettge, I. De Graeve, A. Dugstad, S. Grassini, T. Hack, M. Halama, E.-H. Han, T. Harder, G. Hinds, J. Kittel, R. Krieg, C. Leygraf, L. Martinelli, A. Mol, D. Neff, J.-O. Nilsson, I. Odnevall, S. Paterson, S. Paul, T. Prošek, M. Raupach, R.I. Revilla, F. Ropital, H. Schweigart, E. Szala, H. Terryn, J. Tidblad, S. Virtanen, P. Volovitch, D. Watkinson, M. Wilms, G. Winning, M. Zheludkevich, Corrosion challenges towards a sustainable society, Materials and Corrosion 73(11) (2022) 1730-1751.

[2] R.M. Katona, J.T. Burns, R.F. Schaller, R.G. Kelly, Insights from electrochemical crack tip modeling of atmospheric stress corrosion cracking, Corros. Sci. 209 (2022) 110756.

[3] Y. Zhang, A.J.M.C. Cook, C. Padovani, S. Zhou, A. Turnbull, Atmospheric stress corrosion crack growth rates of 316 L stainless steel for nuclear waste containment, Corros. Sci. 177 (2020) 109008.

[4] E. Akiyama, K. Matsukado, M. Wang, K. Tsuzaki, Evaluation of hydrogen entry into high strength steel under atmospheric corrosion, Corros. Sci. 52 (9) (2010) 2758–2765.

[5] J. Jiang, J. Wang, Y.-h Lu, J.-z Hu, Effect of length of gas/liquid/solid three-phase boundary zone on cathodic and corrosion behavior of metals, Electrochim. Acta 54 (5) (2009) 1426–1435.

[6] T.H. Muster, A. Bradbury, A. Trinchi, I.S. Cole, T. Markley, D. Lau, S. Dligatch, A. Bendavid, P. Martin, The atmospheric corrosion of zinc: The effects of salt concentration, droplet size and droplet shape, Electrochim. Acta 56 (4) (2011) 1866–1873.

[7] A. Nishikata, Y. Ichihara, Y. Hayashi, T. Tsuru, Influence of electrolyte layer thickness and ph on the initial stage of the atmospheric corrosion of iron, J. Electrochem. Soc. 144 (4) (1997) 1244.
[8] B.G. Koushik, N. Van den Steen, M.H. Mamme, Y. Van Ingelgem, H. Terryn, Review on modelling of corrosion under droplet electrolyte for predicting atmospheric corrosion rate, J. Mater. Sci. Technol. 62 (2021) 254–267.
[9] A. Nishikata, Y. Ichihara, T. Tsuru, An application of electrochemical impedance spectroscopy to atmospheric corrosion study, Corros. Sci. 37 (6) (1995) 897–911.
[10] E. McCafferty, Introduction to Corrosion Science, Springer Science & Business Media, 2010.
[11] H. Simillion, N. Van den Steen, H. Terryn, J. Deconinck, Geometry influence on corrosion in dynamic thin film electrolytes, Electrochim. Acta 209 (2016) 149–158.
[12] C.L. Alexander, C. Liu, A. Alshanoon, R.M. Katona, R.G. Kelly, J. Carpenter, C. Bryan, E. Schindelholz, Oxygen reduction on stainless steel in concentrated chloride media, J. Electrochem. Soc. 165 (13) (2018) C869.
[13] S. Li, L. Hihara, The comparison of the corrosion of ultrapure iron and low-carbon steel under NaCl-electrolyte droplets, Corros. Sci. 108 (2016) 200–204.
[14] X. Tang, C. Ma, X. Zhou, X. Lyu, Q. Li, Y. Li, Atmospheric corrosion local electrochemical response to a dynamic saline droplet on pure Iron, Electrochem. Commun. 101 (2019) 28–34.
[15] N. Van den Steen, H. Simillion, D. Thierry, H. Terryn, J. Deconinck, Comparing modeled and experimental accelerated corrosion tests on steel, J. Electrochem. Soc. 164 (9) (2017) C554.
[16] S.M. Gateman, O. Gharbi, M. Turmine, V. Vivier, Measuring changes in wettability and surface area during micro droplet corrosion measurements, Electrochim. Acta 399 (2021) 139402.
[17] E. Dubuisson, P. Lavie, F. Dalard, J.-P. Caire, S. Szunerits, Study of the atmospheric corrosion of galvanised steel in a micrometric electrolytic droplet, Electrochem. Commun. 8 (6) (2006) 911–915.
[18] S. Li, L. Hihara, Atmospheric-corrosion electrochemistry of NaCl droplets on carbon steel, J. Electrochem. Soc. 159 (11) (2012) C461.
[19] R. Oltra, B. Vuillemin, F. Thebault, F. Rechou, Effect of the surrounding aeration on microcapillary electrochemical cell experiments, Electrochem. Commun. 10 (6) (2008) 848–850.
[20] D.B. Blücher, J.-E. Svensson, L.-G. Johansson, M. Rohwerder, M. Stratmann, Scanning Kelvin probe force microscopy: A useful tool for studying atmospheric corrosion of MgAl alloys in situ, J. Electrochem. Soc. 151 (12) (2004) B621.
[21] L. Guo, X. Zhao, B. Wang, Y. Bai, B. Xu, L. Qiao, The initial stage of atmospheric corrosion on interstitial free steel investigated by in situ SPM, Corros. Sci. 70 (2013) 188–193.
[22] C. Senöz, A. Maljusch, M. Rohwerder, W. Schuhmann, SECM and SKPFM Studies of the Local Corrosion Mechanism of Al Alloys – A Pathway to an Integrated SKP-SECM System, Electroanalysis 24 (2) (2012) 239–245.
[23] B. Koushik, N. Van den Steen, H. Terryn, Y. Van Ingelgem, Investigation of the importance of heat transfer during thin electrolyte formation in atmospheric corrosion using a novel experimental approach, Corros. Sci. 189 (2021) 109542.
[24] D.-H. Xia, S. Song, Y. Behnamian, W. Hu, Y.F. Cheng, J.-L. Luo, F. Huet, Review—electrochemical noise applied in corrosion science: theoretical and mathematical models towards quantitative analysis, J. Electrochem. Soc. 167 (8) (2020) 081507.
[25] D.-H. Xia, Y. Ji, R. Zhang, Y. Mao, Y. Behnamian, W. Hu, N. Birbilis, On the localized corrosion of AA5083 in a simulated dynamic seawater/air interface—Part 1: corrosion initiation mechanism, Corros. Sci. 213 (2023) 110985.
[26] D.H. Xia, S.Z. Song, Y. Behnamian, Detection of corrosion degradation using electrochemical noise (EN): review of signal processing methods for identifying corrosion forms, Corrosion Engineering, Sci. Technol. 51 (7) (2016) 527–544.
[27] D.-H. Xia, C.-M. Deng, D. Macdonald, S. Jamali, D. Mills, J.-L. Luo, M.G. Strebl, M. Amiri, W. Jin, S. Song, W. Hu, Electrochemical measurements used for assessment of corrosion and protection of metallic materials in the field: a critical review, J. Mater. Sci. Technol. 112 (2022) 151–183.
[28] D.-H. Xia, C. Ma, S. Song, L. Xu, Detection of atmospheric corrosion of aluminum alloys by electrochemical probes: theoretical analysis and experimental tests, J. Electrochem. Soc. 166 (12) (2019) B1000.
[29] Z. Li, A. Homborg, Y. Gonzalez-Garcia, A. Kosari, P. Visser, A. Mol, Evaluation of the formation and protectiveness of a lithium-based conversion layer using electrochemical noise, Electrochim. Acta 426 (2022) 140733.
[30] A.M. Homborg, E.P.M. Van Westing, T. Tinga, X. Zhang, P.J. Oonincx, G.M. Ferrari, J.H.W. De Wit, J.M.C. Mol, Novel time–frequency characterization of electrochemical noise data in corrosion studies using Hilbert spectra, Corros. Sci. 66 (2013) 97–110.
[31] A.M. Homborg, T. Tinga, E.P.M. Van Westing, X. Zhang, G.M. Ferrari, J.H.W. De Wit, J.M.C. Mol, A critical appraisal of the interpretation of electrochemical noise for corrosion studies, Corrosion 70 (10) (2014) 971–987.
[32] L. Sanchez, T. Fricker, H. Cong, Effect of scale formation and CP potentials on AC-induced pitting corrosion of low carbon steels, J. Mater. Sci. 57 (28) (2022) 13671–13694.
[33] M.D. Deffo Ayagou, T.T. Mai Tran, B. Tribollet, J. Kittel, E. Sutter, N. Ferrando, C. Mendibide, Duret-thual, electrochemical impedance spectroscopy of iron corrosion in H2S solutions, Electrochim. Acta 282 (2018) 775–783, thual, electrthual, electr.
[34] L. Niu, H. Zhang, F. Wei, S. Wu, X. Cao, P. Liu, Corrosion inhibition of iron in acidic solutions by alkyl quaternary ammonium halides: Correlation between inhibition efficiency and molecular structure, Appl. Surf. Sci. 252 (5) (2005) 1634–1642.
[35] F. Farelas, M. Galicia, B. Brown, S. Nesic, H. Castaneda, Evolution of dissolution processes at the interface of carbon steel corroding in a CO2 environment studied by EIS, Corros. Sci. 52 (2) (2010) 509–517.
[36] L. Wang, D. Snihirova, M.D. Havigh, M. Deng, S.V. Lamaka, H. Terryn, M. L. Zheludkevich, Non-stationarity in electrochemical impedance measurement of Mg-based materials in aqueous media, Electrochim. Acta 468 (2023) 143140.
[37] V. Soulié, S. Karpitschka, F. Lequien, P. Prené, T. Zemb, H. Moehwald, H. Riegler, The evaporation behavior of sessile droplets from aqueous saline solutions, Phys. Chem. Chem. Phys. 17 (34) (2015) 22296–22303.
[38] E. Rahimi, A. Rafsanjani-Abbasi, A. Davoodi, A. Kiani-Rashid, Shape evolution of water and saline droplets during icing/melting cycles on superhydrophobic surface, Surf. Coat. Technol. 333 (2018) 201–209.
[39] T.E. Hoffer, S.C. Mallen, Evaporation of contaminated and pure water droplets in a wind tunnel, J. Atmos. Sci. 27 (6) (1970) 914–918.
[40] N. Van Den Steen, Y. Gonzalez-Garcia, J.M.C. Mol, H. Terryn, Y. Van Ingelgem, Predicting the effect of droplet geometry and size distribution on atmospheric corrosion, Corros. Sci. 202 (2022) 110308.
[41] T. Kamimura, K. Kashima, K. Sugae, H. Miyuki, T. Kudo, The role of chloride ion on the atmospheric corrosion of steel and corrosion resistance of Sn-bearing steel, Corros. Sci. 62 (2012) 34–41.
[42] F. Arjmand, A. Adriaens, Influence of pH and chloride concentration on the corrosion behavior of unalloyed copper in NaCl solution: a comparative study between the micro and macro scales, Materials 5 (12) (2012) 2439–2464.
[43] J.P. Duthil, G. Mankowski, A. Giusti, The synergetic effect of chloride and sulphate on pitting corrosion of copper, Corros. Sci. 38 (10) (1996) 1839–1849.
[44] P.M. Natishan, W.E. O'Grady, Chloride Ion Interactions with Oxide-Covered Aluminum Leading to Pitting Corrosion: A Review, J. Electrochem. Soc. 161 (9) (2014) C421.
[45] S. Sharifi-Asl, F. Mao, P. Lu, B. Kursten, D.D. Macdonald, Exploration of the effect of chloride ion concentration and temperature on pitting corrosion of carbon steel in saturated Ca(OH)2 solution, Corros. Sci. 98 (2015) 708–715.
[46] P. Li, M. Du, Effect of chloride ion content on pitting corrosion of dispersion-strengthened-high-strength steel, Corros. Commun. 7 (2022) 23–34.
[47] J.O. Park, S. Matsch, H. Böhni, Effects of temperature and chloride concentration on pit initiation and early pit growth of stainless steel, J. Electrochem. Soc. 149 (2) (2002) B34.
[48] D. Szánto, S. Cleghorn, C. Ponce-de-León, F. Walsh, The limiting current for reduction of ferricyanide ion at nickel: the importance of experimental conditions, AIChE J. 54 (3) (2008) 802–810.
[49] X. Zhong, M. Schulz, C.H. Wu, M. Rabe, A. Erbe, M. Rohwerder, Limiting current density of oxygen reduction under ultrathin electrolyte layers: from the micrometer range to monolayers, ChemElectroChem 8 (4) (2021) 712–718.
[50] A. Schumpe, I. Adler, W.-D. Deckwer, Solubility of oxygen in electrolyte solutions, Biotechnol. Bioeng. 20 (1) (1978) 145–150.
[51] D. Tromans, Modeling oxygen solubility in water and electrolyte solutions, Ind. Eng. Chem. Res. 39 (3) (2000) 805–812.
[52] K. Oldham, J. Myland, A. Bond, Electrochemical Science and Technology: Fundamentals and Applications, John Wiley & Sons, 2011.
[53] V.S. Helbert, A. Nazarov, M. Taryba, F. Vucko, F. Montemor, D. Thierry, Kinetics of corrosion reactions on press hardened steel in atmospheric conditions under thin electrolyte films, Electrochim. Acta 458 (2023) 142500.
[54] D. Landolt, Corrosion and Surface Chemistry of Metals, CRC Press, 2007.
[55] C.L. Alexander, B. Tribollet, M.E. Orazem, Contribution of surface distributions to constant-phase-element (CPE) Behavior: 1. Influence of roughness, Electrochim. Acta 173 (2015) 416–424.
[56] L. Bousselmi, C. Fiaud, B. Tribollet, E. Triki, Impedance spectroscopic study of a steel electrode in condition of scaling and corrosion: interphase model, Electrochim. Acta 44 (24) (1999) 4357–4363.
[57] J. Hu, Sa Cao, J. Xie, EIS study on the corrosion behavior of rusted carbon steel in 3% NaCl solution, Anti-Corros. Methods Mater. 60 (2) (2013) 100–105.
[58] W.R. Osório, L.C. Peixoto, L.R. Garcia, A. Garcia, Electrochemical corrosion response of a low carbon heat treated steel in a NaCl solution, Mater. Corros. 60 (10) (2009) 804–812.
[59] C. Li, Y. Ma, Y. Li, F. Wang, EIS monitoring study of atmospheric corrosion under variable relative humidity, Corros. Sci. 52 (11) (2010) 3677–3686.
[60] G. Kear, B.D. Barker, F.C. Walsh, Electrochemical corrosion of unalloyed copper in chloride media—a critical review, Corros. Sci. 46 (1) (2004) 109–135.
[61] S. Hœrlé, F. Mazaudier, P. Dillmann, G. Santarini, Advances in understanding atmospheric corrosion of iron. II. Mechanistic modelling of wet–dry cycles, Corros. Sci. 46 (6) (2004) 1431–1465.
[62] G. Song, A. Atrens, D.S. John, X. Wu, J. Nairn, The anodic dissolution of magnesium in chloride and sulphate solutions, Corros. Sci. 39 (10) (1997) 1981–2004.
[63] I. Nakatsugawa, R. Martin, E.J. Knystautas, Improving corrosion resistance of AZ91D magnesium alloy by nitrogen ion implantation, Corrosion 52 (12) (1996).
[64] Y. Liu, G.Z. Meng, Y.F. Cheng, Electronic structure and pitting behavior of 3003 aluminum alloy passivated under various conditions, Electrochim. Acta 54 (17) (2009) 4155–4163.
[65] X.-H. Wang, J.-H. Wang, C.-W. Fu, Characterization of pitting corrosion of 7A60 aluminum alloy by EN and EIS techniques, Trans. Nonferrous Met. Soc. China 24 (12) (2014) 3907–3916.
[66] G.A. Zhang, Y.F. Cheng, Localized corrosion of carbon steel in a CO2-saturated oilfield formation water, Electrochim. Acta 56 (3) (2011) 1676–1685.
[67] H. Ma, X. Cheng, S. Chen, G. Li, X. Chen, S. Lei, H. Yang, Theoretical interpretation on impedance spectra for anodic iron dissolution in acidic solutions containing hydrogen sulfide, Corrosion 54 (8) (1998) 634–640.

[68] G.A. Zhang, Y.F. Cheng, Corrosion of X65 steel in CO2-saturated oilfield formation water in the absence and presence of acetic acid, Corros. Sci. 51 (8) (2009) 1589–1595.
[69] M. Jafarian, F. Gobal, I. Danaee, R. Biabani, M.G. Mahjani, Electrochemical studies of the pitting corrosion of tin in citric acid solution containing Cl−, Electrochim. Acta 53 (13) (2008) 4528–4536.
[70] M.A. Jingling, W. Jiuba, L.I. Gengxin, X.V. Chunhua, The corrosion behaviour of Al–Zn–In–Mg–Ti alloy in NaCl solution, Corros. Sci. 52 (2) (2010) 534–539.
[71] K. Xiao, C.-F. Dong, X.-G. Li, F.-M. Wang, Corrosion products and formation mechanism during initial stage of atmospheric corrosion of carbon steel, J. Iron Steel Res. Int. 15 (5) (2008) 42–48.
[72] Y. Hou, C. Aldrich, K. Lepkova, L. Machuca, B. Kinsella, Monitoring of carbon steel corrosion by use of electrochemical noise and recurrence quantification analysis, Corros. Sci. 112 (2016) 63–72.
[73] A. Royani, S. Prifiharni, L. Nuraini, G. Priyotomo, I. Purawiardi, H. Gunawan, Corrosion of carbon steel after exposure in the river of Sukabumi, West Java. IOP Conference Series: Materials Science and Engineering, IOP Publishing, 2019 012031.
[74] D.L. Naik, H.U. Sajid, R. Kiran, G. Chen, Detection of corrosion-indicating oxidation product colors in steel bridges under varying illuminations, shadows, and wetting conditions, Metals 10 (11) (2020) 1439.
[75] S. Choudhary, A. Garg, K. Mondal, Relation between open circuit potential and polarization resistance with rust and corrosion monitoring of mild steel, J. Mater. Eng. Perform. 25 (7) (2016) 2969–2976.
[76] T. Nishimura, Rust formation and corrosion performance of Si- and Al-bearing ultrafine grained weathering steel, Corros. Sci. 50 (5) (2008) 1306–1312.